J. Fluid Mech. (2007), *vol.* 586, *pp.* 1–39. © 2007 Cambridge University Press
doi:10.1017/S0022112007005769 Printed in the United Kingdom

On the front velocity of gravity currents

MARIANO I. CANTERO[1], J. R. LEE[2], S. BALACHANDAR[3]† AND MARCELO H. GARCIA[1]

[1]Department of Civil and Environmental Engineering, University of Illinois at Urbana-Champaign, Urbana, IL 61801, USA

[2]School of Mechanical Engineering, Pusan National University, San 30, Jang Jeon Dong, Kumjung Ku, Busan 609-735, Korea

[3]Department of Theoretical and Applied Mechanics, University of Illinois at Urbana-Champaign, Urbana, IL 61801, USA

(Received 15 February 2006 and in revised form 17 January 2007)

Highly resolved three-dimensional and two-dimensional simulations of gravity currents in planar and cylindrical configurations are presented. The volume of release of the heavy fluid is varied and the different phases of spreading, namely acceleration, slumping, inertial and viscous phases, are studied. The incompressible Navier–Stokes equations are solved assuming that the Boussinesq approximation is valid for small density difference. The simulations are performed for three different Reynolds numbers (Re): 895, 3450 and 8950 (this particular choice corresponds to values of Grashof number: 10^5, 1.5×10^6 and 10^7, respectively). Following their sudden release, the gravity currents are observed to go through an acceleration phase in which the maximum front velocity is reached. As the interface of the current rolls up, the front velocity slightly decreases from the maximum and levels off to a nearly constant value. At higher Re, three-dimensional disturbances grow rapidly and the currents become strongly turbulent. In contrast, in two-dimensional simulations, the rolled-up vortices remain coherent and very strong. Depending on the initial Re of the flow and on the size of the release, the current may transition from the slumping to the inertial phase, or directly to the viscous phase without an inertial phase. New criteria for the critical Re are introduced for the development of the inertial phase. Once the flow transitions to the inertial or viscous phase, it becomes fully three-dimensional. During these phases of spreading, two-dimensional approximations underpredict the front location and velocity. The enhanced vortex coherence of the two-dimensional simulations leads to strong vortex interaction and results in spurious strong time variations of the front velocity. The structure and dynamics of the three-dimensional currents are in good agreement with previously reported numerical and experimental observations.

1. Introduction

Gravity currents (also called density currents) are buoyancy-driven flows which manifest either as a horizontal current of heavy fluid running below light fluid, or as a current of light fluid above heavy fluid. In some applications, the gravity current manifests as a combination of these two, and in this case, they are also called

† Author to whom correspondence should be addressed. Present address: Department of Mechanical and Aerospace Engineering, University of Florida, Gainesville, FL 32611, USA.

intrusions. Gravity currents can be produced with very small density differences (of a few per cent), yet they can still travel for very long distances (García 1992). Examples of these flows are thunderstorm fronts, volcanic eruptions, oil spills on the ocean, and snow avalanches (Allen 1985; Simpson 1997).

The need to predict the arrival time of a gravity current's front and the maximum spreading distance has motivated the development of relatively simple models (Allen 1985) all the way to detailed simulations (Lee & Wilhelmson 1997*a*, *b*; Härtel, Meiburg & Necker 2000*b*; Necker *et al.* 2002, 2005; Özgökmen *et al.* 2004; Cantero *et al.* 2006). The first theoretical attempt to describe the spreading rate of a gravity current using potential flow theory was made by von Kármán (1940). He showed that a deeply submerged heavy fluid current of density ρ_1 will move into a semi-infinite lighter environment of density ρ_0 with a mean front velocity of $u_F = \sqrt{2\,g'\,h_F}$, where $g' = g(\rho_1 - \rho_0)/\rho_0$ is the reduced gravity and h_F is the height of the current. Benjamin (1968) arrived at the same conclusion with a more precise analysis using the theory of hydraulic jumps. Shin, Dalziel & Linden (2004) has shown the importance of including both the front of the gravity current and the backward propagating disturbance in the analysis.

Following experimental observations, Huppert & Simpson (1980) described the spreading of a gravity current in three phases: an initial *slumping phase* where the current moves at nearly constant speed, followed by an *inertial phase* in which the current moves under the balance of buoyancy and inertial forces, and finally a *viscous phase* where viscous effects dominate and balance buoyancy. Power law expressions for the self-similar evolution of the front have been obtained for both the inertial and viscous regimes (Fay 1969). Fannelop & Waldman (1971) and Hoult (1972) have shown that the power law expressions result from a similarity solution of the shallow-water equations and therefore are valid only sufficiently long after the initial release (see also Rottman & Simpson 1983; Bonnecaze, Huppert & Lister 1993; Choi & García 1995; Huppert 1998; Bonnecaze & Lister 1999; Ungarish & Zemach 2003).

Planar and cylindrical gravity currents are two canonical configurations that have been studied in the past. The lock-exchange problem in a rectangular channel is a well-studied example of a planar gravity current, where the heavy fluid moves away from the lock with a nominally straight front. On the other hand, the release of a finite column of heavy fluid into a surrounding ambient of light fluid results in a cylindrical gravity current (Penney *et al.* 1952; Spicer & Havens 1987). In the cylindrical configuration the front is nominally circular and propagates radially outward. In a planar current, as the front propagates, the planform area of the released heavy fluid increases linearly with front location, whereas in a cylindrical current, the planform increases quadratically. This difference changes the spreading rate of the cylindrical current compared to the planar case.

In the lock-exchange problem, as the front of heavy fluid moves away from the lock, a disturbance is also formed which propagates in the opposite direction into the lock. In the case of a finite volume release, this backward-propagating disturbance reflects off the back wall, or the symmetry plane, and begins to propagate forward. The reflected disturbance travels faster than the front of the gravity current, eventually catching up with the front. The near constant velocity of the current (the slumping phase) continues up to this point and, as observed by Rottman & Simpson (1983), the arrival of the reflected wave at the front initiates the transition to the inertial phase. The volume of heavy fluid (per unit width of the channel) released behind the lock plays an important role as to when this transition to the inertial phase occurs. In the limit of an infinite release, the slumping phase persists indefinitely for high

Reynolds numbers (Re). At lower Re, viscous effects will eventually reduce the front velocity, and in the case of finite releases the inertial phase may not exist at all, and the current may directly transition from the slumping phase to the viscous phase (Rottman & Simpson 1983; Amy *et al.* 2005). Although the physical mechanism of this transition has not been nearly as well understood, it can be expected that the volume of release will also play a role as to when such direct transition from the slumping to the viscous phase will occur.

If the effect of the sidewalls can be neglected, then the planar current can be considered statistically two-dimensional and homogeneous along the spanwise direction. Similarly, a cylindrical current is statistically axisymmetric and homogeneous along the circumferential direction. The two-dimensionality of the planar current and the axisymmetry of the cylindrical current have been exploited both in theoretical formulations and in computations (Daly & Pracht 1968; Droegemeier & Wilhelmson 1986, 1987; Terez & Knio 1998*a*, *b*; Hallworth, Huppert & Ungarish 2001; Özgökmen & Chassignet 2002; Ungarish & Zemach 2003; Birman, Martin & Meiburg 2005; Patterson *et al.* 2006). At high Re, gravity currents are strongly three-dimensional and fully turbulent. In such situations, the two-dimensionality or the axisymmetry of the current is only in a statistical sense.

The effect of three-dimensionality on the speed of the current can be expected to be significant. For example, Cantero (2002) and Cantero *et al.* (2003) reported numerical simulations of planar gravity currents developing over a favourable slope and compared the results with experimental data. They found that a three-dimensional simulation captures the experimental observations more accurately and that the two-dimensional model lags behind. Similar results have been reported by Necker *et al.* (2002) in the context of particulate gravity currents. Considering the front of the heavy fluid as a bluff body intruding into the light fluid, a crude analogy with the drag force on a cylindrical body subjected to crossflow can be drawn for which two-dimensional model significantly overpredicts the drag force (Mittal & Balachandar 1995). Thus, a weaker resistance to the flow can be expected in the case of a three-dimensional front than for the case of a coherent two-dimensional front, which could explain the faster spreading of three-dimensional currents.

The primary objective of the present work is to study systematically the propagation of gravity currents and to investigate the influence of key parameters on the front velocity as well as the transition between phases. In this work, we present results from highly resolved simulations of planar and cylindrical gravity currents for varying Re. For the planar case, we consider both small and large release volumes. A detailed comparison of the results illustrates the role of the planar *vs.* cylindrical nature of the current, as well as the effect of the volume of release on the mean velocity of the front and the transition between the different phases. In each of these cases we consider both fully resolved three-dimensional simulations and corresponding two-dimensional or axisymmetric simulations for planar and cylindrical configurations, respectively. The three-dimensional structure of the propagating front is also explored for both the planar and cylindrical configurations.

2. Numerical formulation

The physical configuration of the gravity currents is shown in figure 1. At the start of the computation the region with heavy fluid of density ρ_1 (the shaded region in figure 1) is separated from the light fluid of density ρ_0. In the planar case, the heavy fluid is a slab of half-width x_0 along the flow direction. In the present simulations, the

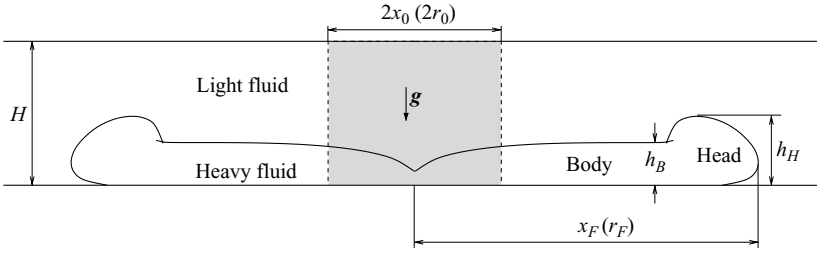

FIGURE 1. Sketch of a gravity current and the nomenclature used in this work. The flow is started from the initial condition shown by the shaded region between dashed lines. As the flow evolves, the intruding front develops the structure of a head followed by a body.

slab of heavy fluid extends over the entire height H of the channel (full-depth release) and infinitely along the spanwise (y) direction. In the cylindrical case, the region of heavy fluid is a cylinder of radius r_0 and height H.

We consider flows in which the density difference is small enough that the Boussinesq approximation is valid. The dimensionless equations read

$$\frac{\partial \tilde{u}_i}{\partial \tilde{t}} + \tilde{u}_k \frac{\partial \tilde{u}_i}{\partial \tilde{x}_k} = \tilde{\rho}\, e_i^g - \frac{\partial \tilde{p}}{\partial \tilde{x}_i} + \frac{1}{Re} \frac{\partial^2 \tilde{u}_i}{\partial \tilde{x}_k \partial \tilde{x}_k}, \tag{2.1}$$

$$\frac{\partial \tilde{u}_k}{\partial \tilde{x}_k} = 0, \tag{2.2}$$

$$\frac{\partial \tilde{\rho}}{\partial \tilde{t}} + \frac{\partial}{\partial \tilde{x}_k} (\tilde{\rho} \tilde{u}_k) = \frac{1}{Sc\, Re} \frac{\partial^2 \tilde{\rho}}{\partial \tilde{x}_k \partial \tilde{x}_k}. \tag{2.3}$$

Here, $\tilde{u}_i$ is the dimensionless velocity vector, and e_i^g is a unit vector pointing in the gravity direction. Any variable with a tilde is to be understood as dimensionless.

The channel height H is the length scale and we adopt $U = \sqrt{g'H}$ as the velocity scale. Consequently, the time scale is H/U. The dimensionless density and pressure are given by

$$\tilde{\rho} = \frac{\rho - \rho_0}{\rho_1 - \rho_0}, \qquad \tilde{p} = \frac{p}{\rho_0 U^2}. \tag{2.4}$$

The two dimensionless parameters in equations (2.1)–(2.3) are the Reynolds and Schmidt numbers defined as

$$Re = \frac{U\,H}{\nu} = \sqrt{\frac{g' H^3}{\nu^2}}, \qquad Sc = \frac{\nu}{\kappa}, \tag{2.5}$$

respectively, where ν is the kinematic viscosity and κ is the diffusivity of temperature or chemical species producing the density difference. The ratios x_0/H (planar case) or r_0/H (cylindrical case) are additional geometric parameters that control the volume of initial release. In the planar configuration, we consider the cases of both a small volume of release with $\tilde{x}_0 = 1$ (*small-release* case) and a large volume of release with $\tilde{x}_0 = \tilde{L}_x/4$ (*large-release* case), where $\tilde{L}_x$ is the length of the computational domain in the spreading direction. Thus, in the large-release simulations, half the computational domain is filled with the heavy fluid and serves to approximate the infinite-release case.

In the three-dimensional planar simulations, the governing equations are solved in a rectangular box of size $\tilde{L}_x \times \tilde{L}_y \times \tilde{L}_z$. Periodic boundary conditions are employed along the streamwise ($\tilde{x}$) and spanwise ($\tilde{y}$) directions. Periodicity along the streamwise direction implies that a periodic array of planar gravity currents, each initially separated by a distance $\tilde{L}_x$, is being simulated. The box is typically taken to be very

Geometry (domain size)		*Re*		
		895	3450	8950
Planar (large release setting)	Two-dimensional (34×1)	Spectral (1056×80)	Spectral (1280×110)	Spectral (2048×180)
	Three-dimensional ($34 \times 1.5 \times 1$)	Spectral ($1056 \times 64 \times 80$)	Spectral ($1280 \times 84 \times 110$)	Spectral ($2048 \times 112 \times 180$)
Planar (small release setting)	Two-dimensional (25×1)	Spectral (768×80)	Spectral (924×110)	Spectral (1536×180)
	Three-dimensional ($25 \times 1.5 \times 1$)	Spectral ($768 \times 64 \times 80$)	Spectral ($924 \times 84 \times 110$)	Spectral ($1536 \times 112 \times 180$)
Cylindrical (small release setting)	Axisymmetry (7.5×1)	Multi-domain (408×71)	Multi-domain (568×111)	Multi-domain (1572×201)
	Three-dimensional ($15 \times 15 \times 1$)	Spectral* ($280 \times 280 \times 72$)	Spectral ($512 \times 512 \times 110$)	Spectral ($880 \times 880 \times 180$)

TABLE 1. Numerical simulations performed for this study. The size of the domain, numerical method and resolution is specified for each geometrical setting. The size of the domain is specified as $(\tilde{L}_x \times \tilde{L}_y \times \tilde{L}_z)$ in the three-dimensional configuration, as $(\tilde{L}_x \times \tilde{L}_z)$ in the two-dimensional planar configuration, and as $(\tilde{L}_r \times \tilde{L}_z)$ in the axisymmetric configuration. The resolution is specified as $(N_x \times N_y \times N_z)$ in the three-dimensional configuration, as $(N_x \times N_z)$ in the two-dimensional planar configuration, and as $(N_r \times N_z)$ in the axisymmetric configuration. *The domain size for this run is $(10 \times 10 \times 1)$.

long along the streamwise direction (25 or more channel heights) in order to allow free unhindered development of the current for a long time (see figure 1). Based on simulation results, we observe that the interaction of the front with the adjacent currents across the periodic boundaries can be neglected until the front reaches about 1 dimensionless unit from the boundaries. Along the spanwise direction, the width of the periodic domain is chosen to be 1.5 dimensionless units, which is adequate for including several spanwise lobe and cleft structures. These choices for the computational domain are consistent with that of Härtel *et al.* (2000*b*).

The three-dimensional cylindrical simulations are also in a rectangular box of size $\tilde{L}_x \times \tilde{L}_y \times \tilde{L}_z$; however, since the current spreads radially outward along the entire $(\tilde{x}, \tilde{y})$-plane, we choose $\tilde{L}_x = \tilde{L}_y$. Periodic boundary conditions are employed along the $(\tilde{x})$ and $(\tilde{y})$ directions and thus here we approximate a doubly periodic array of cylindrical gravity currents with a lateral spacing of $\tilde{L}_x = \tilde{L}_y$ along the horizontal directions. The planform of the periodic box is typically taken to be very large (15 channel heights) in order to allow unhindered development of the current for a long time. As in the planar case, the interaction of the radially advancing front with the adjacent currents across the periodic boundaries becomes significant only as the front reaches to within 1 dimensionless unit of the boundaries.

The two-dimensional planar simulations are in a rectangular domain of size $\tilde{L}_x \times \tilde{L}_z$ and the flow is taken to be invariant along the spanwise $(\tilde{y})$ direction. The axisymmetric cylindrical simulations are on the $(\tilde{r}, \tilde{z})$ (radial–axial)-plane in a rectangular computational domain of size $\tilde{L}_r \times \tilde{L}_z$, and the flow is invariant along the circumferential (θ) direction.

In this work, we have employed two different numerical techniques: a spectral multi-domain code (Deville, Fischer & Mund 2002) and a fully de-aliased pseudo-spectral code (Canuto *et al.* 1988). The spectral multi-domain code was used to simulate axisymmetric cylindrical currents whereas the spectral code was used in all other simulations. Table 1 gives all the simulations to be discussed in this paper.

In the spectral code, Fourier expansions are employed for the flow variables along the horizontal directions ($\tilde{x}$ and $\tilde{y}$). In the inhomogeneous vertical direction ($\tilde{z}$), a Chebyshev expansion is used with Gauss–Lobatto quadrature points (Canuto *et al.* 1988). The flow field is time advanced using a Crank–Nicolson scheme for the diffusion terms. The advection terms are handled with the Arakawa method (Durran 1999) and advanced with a third-order Runge–Kutta scheme. The buoyancy term is also advanced with a third-order Runge–Kutta scheme. More details on the implementation of this numerical scheme can be found in Cortese & Balachandar (1995). In the simulations, periodic boundary conditions are enforced along the horizontal directions for all variables. At the top and bottom walls, no-slip and zero-gradient conditions are enforced for velocity and density, respectively.

The spectral multi-domain code employs a domain decomposition methodology along the radial direction ($\tilde{r}$) (Balachandar & Parker 2002). The entire computational domain of length $\tilde{L}_r$ is divided into N_e subdomains. Within each subdomain, Chebyshev expansions are used along both radial ($\tilde{r}$) and vertical ($\tilde{z}$) directions. The nonlinear and buoyancy terms are treated explicitly using the third-order Adams–Bashforth scheme. The diffusion terms are treated implicitly with the Crank–Nicolson scheme. Appropriate symmetry boundary conditions are employed for all variables along the centreline ($\tilde{r}=0$). At the outer radial boundary ($\tilde{r}=\tilde{L}_r$), a non-reflecting outflow boundary is used (Mittal & Balachandar 1996). The two different codes were verified to yield identical results for the two-dimensional planar problem.

In all the configurations, the initial density was smoothly varied from 0 to 1 over a thin region located at the interface. The details of the initial conditions used in this work can be found in Cantero *et al.* (2006). The flow was started from rest with a minute random disturbance prescribed in the density field.

In this work, three different Re are considered: $Re=895$, 3450 and 8950. These correspond to Grashof numbers of 10^5, 1.5×10^6 and 10^7, respectively, and the intermediate case can be directly compared with that of Härtel *et al.* (2000*b*). As will be discussed below, with increasing Re, the complexity of the flow increases and thus, the simulation at the higher Re requires increased resolution. The numerical resolution for each simulation was selected to have between 6 and 8 decades of decay in the energy spectrum for all the variables. The time step was selected to produce a Courant number smaller than 0.5.

3. Theoretical background

Several theoretical and empirical models have been proposed to predict the front velocity during the slumping, inertial and viscous phases of the current. In this section, we will briefly describe some of the models that are of immediate relevance to the subsequent discussion.

3.1. *Slumping phase*

Benjamin (1968) analysed the flow in a planar two-dimensional emptying cavity using the hydraulic theory in a frame of reference moving with the front. The only free parameter is the ratio of the depth of the current (h_F) to the depth of the ambient fluid (H). The theory does not distinguish between head height and body height and, in relation to figure 1, $h_B=h_H=h_F$. Benjamin derived the following expression for the Froude number of the front

$$F_B=\frac{u_F}{\sqrt{g'H}}=\left[\tilde{h}_F(2-\tilde{h}_F)\left(\frac{1-\tilde{h}_F}{1+\tilde{h}_F}\right)\right]^{1/2}, \tag{3.1}$$

where $\tilde{h}_F = h_F/H$ is the dimensionless current height and u_F is the dimensional front velocity. Benjamin argued that without external energy input, the largest possible current height can only be $h_F = H/2$. In this limit of $\tilde{h}_F \to 1/2$, $F_B \to 1/2$, and energy losses are associated with currents of smaller depth. Benjamin further argued that dissipation is an essential ingredient of gravity current flow and therefore $h_F/H \leqslant 0.347$. With $h_F/H = 0.347$, a maximum dissipation is achieved within Benjamin's framework.

Shin *et al.* (2004) revisited and extended Benjamin's theory and stressed the need to take into account the exchange between the advancing front of the gravity current and the backward-propagating disturbance. They showed that for both the full-depth and partial-depth lock-exchange releases, the height of an energy-conserving current is half the initial depth of the release. The corresponding speed of the current depends only on the dimensionless initial depth of the release ($\tilde{D}$)

$$F_S = \tfrac{1}{2}\sqrt{\tilde{D}(2-\tilde{D})}. \tag{3.2}$$

The Froude number definition in (3.2) is the same as in (3.1) and the subscripts B and S indicate relations proposed by Benjamin (1968) and Shin *et al.* (2004). In the limit of full-depth release (i.e. $\tilde{D} \to 1$), the above expression yields the same Froude number as Benjamin's expression.

Based on experimental measurements, Huppert & Simpson (1980) proposed the following empirical expression for the Froude number (defined as in (3.1)):

$$F_{HS} = \begin{cases} \tfrac{1}{2}\tilde{h}_F^{1/6} & \text{if } 0.075 \leqslant \tilde{h}_F \leqslant 1, \\ 1.19\,\tilde{h}_F^{1/2} & \text{if } 0 \leqslant \tilde{h}_F \leqslant 0.075, \end{cases} \tag{3.3}$$

where $\tilde{h}_F$ is to be interpreted as the dimensionless height of the body of the current. This empirical expression predicts that the Froude number monotonically decreases to zero as the height of the current decreases to zero. Equation (3.3) yields $F_{HS} = (1/2)^{7/6}$ in the limit $\tilde{h}_F \to 1/2$, which is somewhat lower than the value $1/2$ predicted by the hydraulic theories of both Benjamin (1968) and Shin *et al.* (2004). In the limit of deeply submerged current ($\tilde{h}_F \to 0$), (3.3) yields $F_{HS} \to 1.19\sqrt{\tilde{h}_F}$, which is higher than $F_S \to \sqrt{\tilde{h}_F}$ predicted by Shin *et al.* (2004), but lower than $F_B \to \sqrt{2\tilde{h}_F}$ predicted by Benjamin (1968).

3.2. *Inertial phase*

Transition from the slumping to the inertial phase occurs when the reflected back-propagating wave catches up with the front (Rottman & Simpson 1983). It is accepted that for a planar current, the transition happens after the front has travelled between 5 and 9 lock lengths (Rottman & Simpson 1983; Metha, Sutherland & Kyba 2002; Marino, Thomas & Linden 2005). The asymptotic behaviour of the current in the inertial phase has been established to be (Fay 1969; Fannelop & Waldman 1971; Hoult 1972; Huppert & Simpson 1980; Rottman & Simpson 1983)

$$\tilde{x}_F = \xi_p\,(\tilde{h}_0\tilde{x}_0\,\tilde{t}^{\,2})^{1/3}, \qquad \tilde{u}_F = \tfrac{2}{3}\xi_p(\tilde{h}_0\tilde{x}_0)^{1/3}\tilde{t}^{-1/3} \tag{3.4}$$

for planar currents, and

$$\tilde{r}_F = \pi^{1/4}\xi_c\,\tilde{h}_0^{1/4}(\tilde{r}_0\,\tilde{t})^{1/2}, \qquad \tilde{u}_F = \tfrac{1}{2}\pi^{1/4}\xi_c\tilde{h}_0^{1/4}\tilde{r}_0^{1/2}\tilde{t}^{-1/2} \tag{3.5}$$

for cylindrical currents. Here, $\tilde{x}_F$ and $\tilde{r}_F$ are the dimensionless streamwise and radial location of the planar and cylindrical currents, respectively. The initial size of the release is characterized by its height $\tilde{h}_0$, and length $\tilde{x}_0$ or radius $\tilde{r}_0$. The difference

between the theories is in the constants ξ_p and ξ_c. For the planar current, $\xi_p = 1.6$ and 1.47 have been proposed by Hoult (1972) and Huppert & Simpson (1980), respectively, whereas Marino *et al.* (2005) suggests a range from 1.35 to 1.8. For the cylindrical current, Hoult (1972) and Huppert & Simpson (1980) have proposed $\xi_c = 1.3$ and 1.16, respectively.

3.3. *Viscous phase*

By balancing the buoyancy and viscous forces in a boundary-layer approximation, Hoult (1972) obtained the following self-similar solution for a planar gravity current

$$\tilde{x}_F = \xi_{pHt}\,\tilde{h}_0^{1/2}\,\tilde{x}_0^{1/2}\,Re^{1/8}\,\tilde{t}^{\,3/8}, \qquad \tilde{u}_F = \tfrac{3}{8}\xi_{pHt}\,\tilde{h}_0^{1/2}\,\tilde{x}_0^{1/2}\,Re^{1/8}\,\tilde{t}^{\,-5/8}, \tag{3.6}$$

where $\xi_{pHt} = 1.5$. The corresponding results for a cylindrical current are

$$\tilde{r}_F = \xi_{cHt}\,\tilde{h}_0^{1/3}\,\tilde{r}_0^{2/3}\,Re^{1/12}\,\tilde{t}^{\,1/4}, \qquad \tilde{u}_F = \tfrac{1}{4}\xi_{cHt}\,\tilde{h}_0^{1/3}\,\tilde{r}_0^{2/3}\,Re^{1/12}\,\tilde{t}^{\,-3/4}, \tag{3.7}$$

where $\xi_{cHt} = 1.38$. The viscous force considered in the analysis of Hoult (1972) is from the interface between the heavy and light fluids. A revised analysis that accounts for the viscous effect over a rigid horizontal surface was performed by Huppert (1982). The resulting self-similar solutions for the viscous phase are different from those given in (3.6) and (3.7), and are given by

$$\tilde{x}_F = \xi_{pHp}\,\tilde{h}_0^{3/5}\,\tilde{x}_0^{3/5}\,Re^{1/5}\,\tilde{t}^{\,1/5}, \qquad \tilde{u}_F = \tfrac{1}{5}\xi_{pHp}\,\tilde{h}_0^{3/5}\,\tilde{x}_0^{3/5}\,Re^{1/5}\,\tilde{t}^{\,-4/5}, \tag{3.8}$$

for planar currents where $\xi_{pHp} = 1.133$, and by

$$\tilde{r}_F = \xi_{cHp}\,\tilde{h}_0^{3/8}\,\tilde{r}_0^{3/4}\,Re^{1/8}\,\tilde{t}^{\,1/8}, \qquad \tilde{u}_F = \tfrac{1}{8}\xi_{cHp}\,\tilde{h}_0^{3/8}\,\tilde{r}_0^{3/4}\,Re^{1/8}\,\tilde{t}^{\,-7/8} \tag{3.9}$$

for a cylindrical current where $\xi_{cHp} = 1.197$.

4. Results and discussion

4.1. *Current height*

The height of the current can be defined in a few different ways. Shin *et al.* (2004) and Marino *et al.* (2005) define a local equivalent height in an unambiguous way as

$$\tilde{h}(\tilde{x}, \tilde{y}, \tilde{t}) = \int_0^1 \tilde{\rho}\,\mathrm{d}\tilde{z}\,, \tag{4.1}$$

and this definition is adopted herein. Thus, at locations where the entire layer is occupied by the heavy fluid, the dimensionless height is unity, whereas at locations where the light fluid fills the entire layer, the height is zero. The local current height can then be averaged over the span in the case of a three-dimensional planar current, or along the circumferential direction in the case of a three-dimensional cylindrical current, to define the span-averaged current height as

$$\overline{h}(\tilde{x}, \tilde{t}) = \frac{1}{\tilde{L}_y}\int_0^{\tilde{L}_y} \tilde{h}\,\mathrm{d}\tilde{y} \qquad \text{or} \qquad \overline{h}(\tilde{r}, \tilde{t}) = \frac{1}{2\pi}\int_0^{2\pi} \tilde{h}\,\mathrm{d}\theta\,. \tag{4.2}$$

(Any variable with an overbar is to be understood as dimensionless span-averaged quantity.) The above definition for the planar current is equivalent to the width-averaged dye concentration obtained in experiments (Shin *et al.* 2004; Marino *et al.* 2005).

Figure 2 shows the time evolution of the large-release planar gravity current at *Re* 895 and 8950 plotted in terms of the span-averaged equivalent current height. The

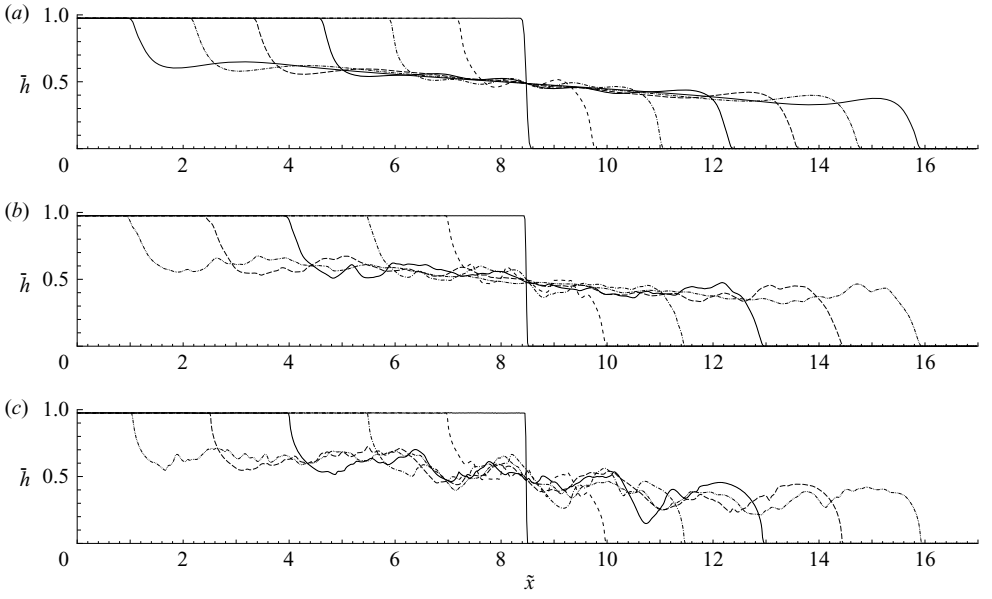

FIGURE 2. Time evolution of the large-release planar gravity current plotted in terms of the span-averaged equivalent current height as defined by (4.2). Contours are shown with time intervals of 3.54 time units. (*a*) Three-dimensional simulation for $Re = 895$; (*b*) three-dimensional simulation for $Re = 8950$; (*c*) two-dimensional simulation for $Re = 8950$.

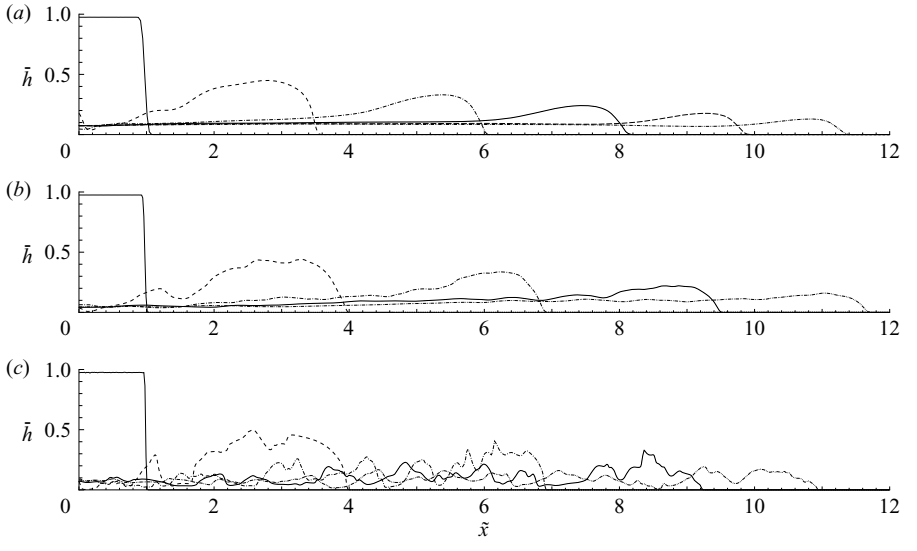

FIGURE 3. As for figure 2, but for small-release planar gravity current and time intervals of 7.08 time units.

corresponding results for the small-release planar current and cylindrical current are shown in figures 3 and 4, respectively. At $Re = 895$ both the planar and cylindrical currents are laminar and remain two-dimensional and axisymmetric, respectively. At the higher Re, the currents are highly three-dimensional and appear turbulent at both the head and over the entire body of the current. Here, the results for both the

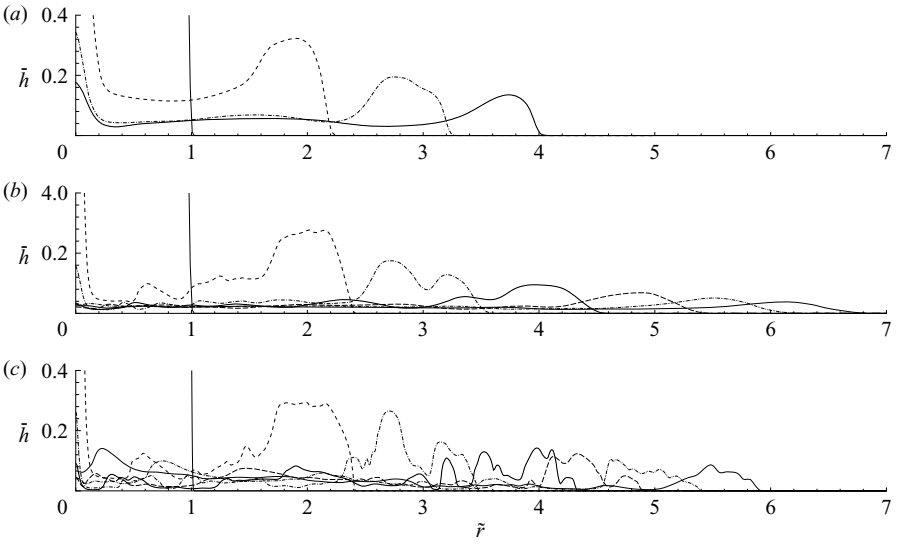

FIGURE 4. Time evolution of the cylindrical gravity current plotted in terms of the circumferentially averaged equivalent current height as defined by (4.2). Contours are shown with time intervals of 3.54 time units. (*a*) Three-dimensional simulation for $Re = 895$; (*b*) three-dimensional simulation for $Re = 8950$; (*c*) axisymmetric simulation for $Re = 8950$.

two-dimensional (or axisymmetric in case of cylindrical current) and three-dimensional simulations, are plotted.

At the lower Re, the current appears smooth with a well-defined raised head and an extended body. In the large-release cases (figure 2) the height of the raised head can be observed to be less than half the initial depth of release and can be observed to slowly decrease with time. After a short dip behind the head, the height of the current gently increases to half the channel height (by symmetry $\tilde{h} = 0.5$ at $\tilde{x} = 8.5$). Birman *et al.* (2005) reported similar results for large-release currents with slip boundary conditions from two-dimensional highly resolved simulations. Here we extend these results to two more cases (planar small-release and cylindrical) for two-dimensional and three-dimensional simulations with no-slip boundary conditions. In the small-release cases, the current has a well-defined raised head and an extended body of near constant height, which can be discerned well at later times. Also at early times, a backward-travelling disturbance wave can be seen as a second peak, which reflects back off the symmetry plane ($\tilde{x} = 0$ or $\tilde{r} = 0$). At later times, it is difficult to identify this reflected disturbance unambiguously. Nevertheless, it is likely that such a disturbance catches up with the front and influences the propagation speed (see Simpson 1982; Rottman & Simpson 1983).

At the higher Re, very large undulations can be seen in the height of the current at early times. These undulations are the result of strong roll-up of the current owing to Kelvin–Helmholtz instability of the shear layer. At much later times, the strong effect of roll-up observed during the early stages of the current is somewhat mitigated and the undulations in the current height are reduced. The effect of roll-up is much stronger in the two-dimensional simulations, since three-dimensionality helps to break up the spanwise or circumferential coherence. The averaged structure and evolution of the large- and small-release currents seen in figures 2 and 3 are qualitatively similar to the width-averaged experimental results of Shin *et al.* (2004)

and Marino *et al.* (2005), respectively. At higher Re, when the flow is highly turbulent, the three-dimensional small-release front arrives earlier than the corresponding two-dimensional or axisymmetric approximation (see figures 3 and 4). This observation suggests that the three-dimensional currents are faster than the two-dimensional (or axisymmetric) approximations.

4.2. *Mean front location and velocity*

The mean front location, $\overline{x}_F(t)$ (or $\overline{r}_F(t)$), can be unambiguously defined as the location where the span-averaged equivalent height, $\overline{h}$, becomes smaller than a small threshold δ. Diffusion and numerical noise prevents $\overline{h}$ from being exactly zero. The above definition is insensitive to the exact value of δ as long as it is smaller than 0.05, and here we use $\delta = 0.01$. The distance the front has advanced, $\overline{x}_F - \overline{x}_0$ (or $\overline{r}_F - \overline{r}_0$), is shown as a function of time in figure 5. The result for all the two-dimensional and three-dimensional large-release planar cases at the three different Re are shown in figure 5(a). The corresponding results for the small-release planar and the cylindrical currents are shown in figures 5(b) and 5(c), respectively. In the log–log plots, the dashed straight line corresponds to a slope of constant front velocity. It can be seen that in all the planar cases, after a brief initial period of acceleration, a period of near constant velocity is realized. The constant velocity, however, seems to depend on Re, at least over the limited range under consideration. Although subtle, departure from the constant velocity can be observed at later times for the small-release cases. The large-release cases continue to exhibit constant velocity over the entire duration of simulation. For the cylindrical cases, a period of constant velocity is not clearly identified. There is, however, a brief period of rather slower variation before the more pronounced decay.

The mean front velocity is computed as

$$\overline{u}_F = \frac{\mathrm{d}\overline{x}_F}{\mathrm{d}\tilde{t}} \tag{4.3}$$

for planar cases and in an analogous way for the cylindrical configurations. The front velocity as a function of $\tilde{t}$ for the large-release planar cases is shown in the inset of figure 5(a). The front velocity of the small-release planar and cylindrical currents are shown in the insets in figures 5(b) and 5(c), respectively. An acceleration phase where the velocity sharply increases, a slumping phase where the velocity is nearly constant (planar currents) or varies rather slowly (cylindrical currents), and an inertial and/or viscous phase where the front velocity decays are clearly identifiable. In what follows, these different phases will be discussed in greater detail.

4.2.1. *Acceleration phase*

In the acceleration phase, the front velocity rapidly increases from zero, reaches a maximum and subsequently falls slightly before approaching a constant value. This early stage of the flow was also observed in experiments by Martin & Moyce (1952a, b) and in two-dimensional simulations by Härtel, Meiburg & Necker (1999). Here, we extend the analysis to three-dimensional simulations, and link the process to the current interface roll-up dynamics. With our simulations, we study the idealized case of an instantaneous release with the gate lifted infinitely rapidly. Nevertheless, the study of this phase is important because it puts in evidence the effect of interface friction on the front speed. During this phase of spreading, three-dimensional disturbances introduced into the current in the initial condition have not grown to sufficient amplitude and the currents are therefore predominantly two-dimensional

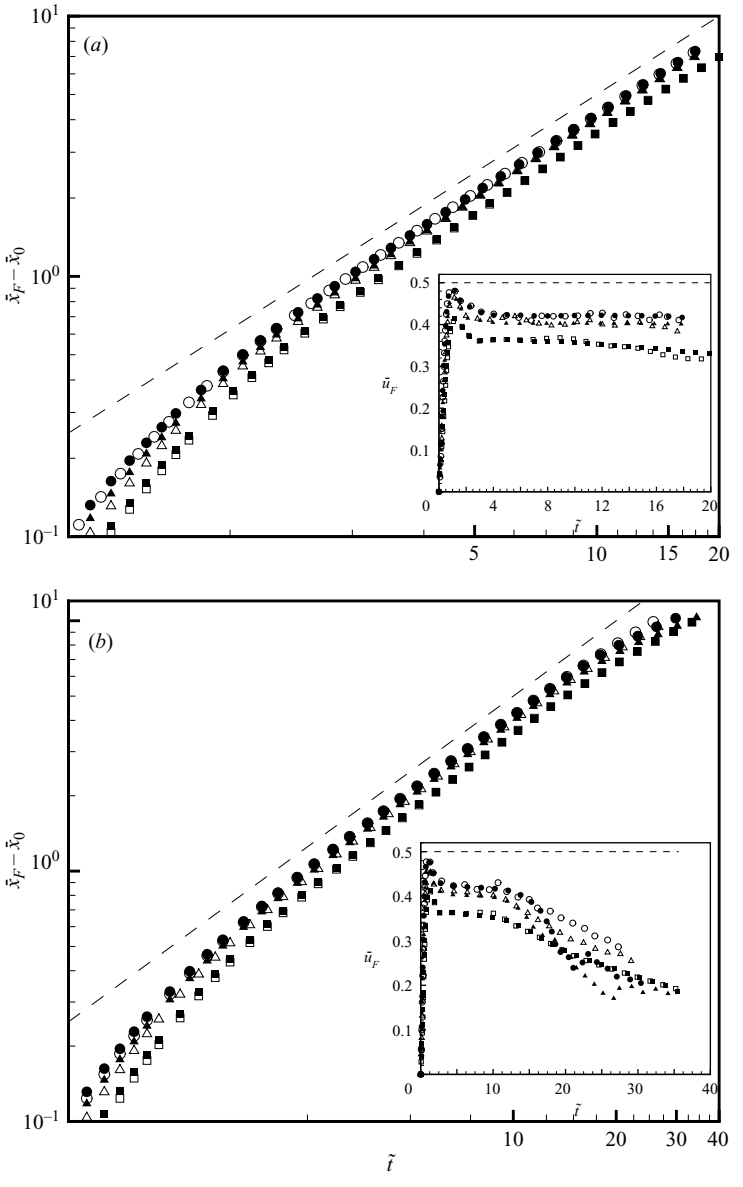

FIGURE 5(*a*, *b*). For caption see facing page.

(or axisymmetric). Thus, the velocities of the current predicted by three-dimensional and two-dimensional simulations are nearly identical in all cases considered.

Figure 6 shows the front velocity as a function of the distance travelled by the front during the acceleration phase. The maximum front velocity increases with increasing Re. In the large-release planar cases, the peak values of the front velocity are 0.411, 0.465 and 0.489 at $Re = 895$, 3450 and 8950, respectively. Based on this trend, the peak front velocity can be expected to level off and become Re-independent at even higher Re. Furthermore, in all the planar and cylindrical cases, the peak front velocity occurs at a distance of about $0.3H$ from the lock-location (see figure 6). This result is independent of the volume released or the strength of the current (i.e. Re of the

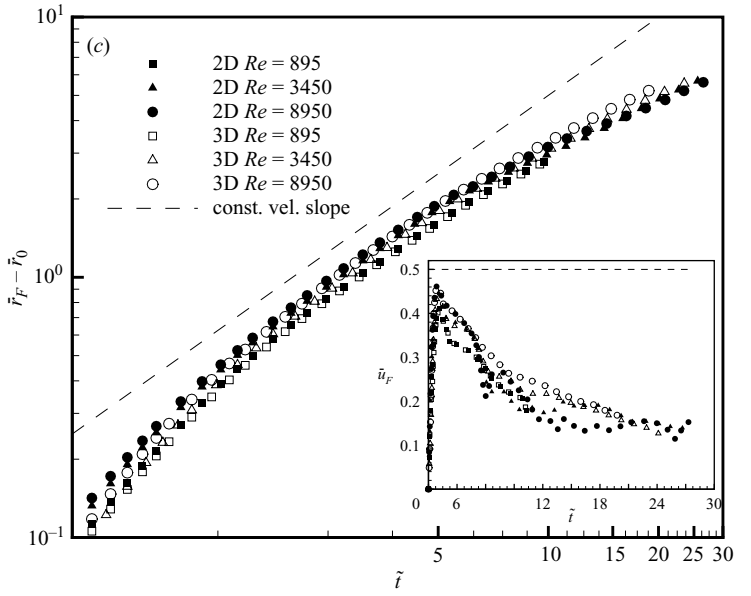

FIGURE 5. Time evolution of front location for all the simulations in table 1. (*a*) Large-release planar current; (*b*) small-release planar current; (*c*) cylindrical current. The dashed lines represent a constant velocity spreading slope, that is $\overline{x}_F - \overline{x}_0 \approx \tilde{t}$ or $\overline{r}_F - \overline{r}_0 \approx \tilde{t}$. The insets show the corresponding time evolution of the front velocity. For the insets, the dashed lines represent the theoretical value from the hydraulic theories of Benjamin (1968) and Shin *et al.* (2004) developed for planar currents.

current) for the conditions of our simulations. In terms of time, at $Re = 8950$, the peak occurs at about one dimensionless time unit after the release, but at lower Re, the peak occurs slightly later, because of the lower current speed.

The cylindrical currents also go through a peak in the front velocity; however, these peaks are, in general, lower than the corresponding planar values. The Re values for the different simulations presented in table 1 are based on initial conditions. As the current advances from the lock, the effective depth of the heavy fluid decreases and the instantaneous Re, defined based on this effective depth, also decreases. At the instance of peak velocity, using the definition of Re (equation (2.5)) and the mass balances $\overline{x}_0 \overline{h}_0 = \overline{x}_F \overline{h}_F$ and $\overline{r}_0^2 \overline{h}_0 = \overline{r}_F^2 \overline{h}_F$, an instantaneous Re can be defined as

$$Re_{peak} = Re(\overline{x}_0/\overline{x}_{peak})^{3/2}, \qquad Re_{peak} = Re(\overline{r}_0/\overline{r}_{peak})^3, \tag{4.4}$$

for the planar and the cylindrical cases, respectively. If we use the fact that $\overline{x}_{peak} - \overline{x}_0 \approx \overline{r}_{peak} - \overline{r}_0 \approx 0.3$, then the instantaneous Re at the timess of peak velocity are about 1.5 and 2.2 times lower than the initial Re for the small-release planar and cylindrical currents, respectively. Owing to the quadratic increase in planform area as it advances, the strength of the cylindrical current measured in terms of instantaneous Re falls off more rapidly. The observed lower peak velocity for the cylindrical current is consistent with its faster decay in strength. In the large-release planar cases, owing to the large initial release volume ($\overline{x}_0 = 8.5$), we now have $\overline{x}_{peak}/\overline{x}_0 \approx 1.04$. As a result, at the time of peak velocity, the instantaneous Re has fallen by only 6%. The inset in figure 6 shows a log–log plot of the peak velocity, $\overline{u}_{F,peak}$, as a function of the Re_{peak}. There is better collapse of $\overline{u}_{F,peak}$ as a function of Re_{peak}. Admittedly the above

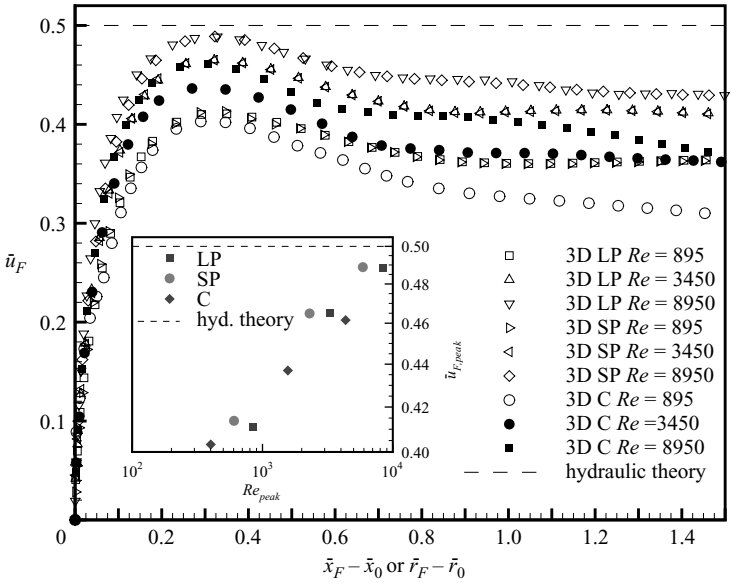

FIGURE 6. Front velocity during the acceleration phase as a function of distance travelled for all the simulations in table 1. The dashed line represents the theoretical value from the hydraulic theory by Benjamin (1968) and Shin *et al.* (2004). The maximum of the front velocity is reached at $\bar{x}_F - \bar{x}_0 \approx 0.33$, regardless of geometrical configuration and Re. LP, large-release planar current; SP, small-release planar current; C, cylindrical current. The inset figure shows the peak velocity, $\bar{u}_{F,peak}$, in the acceleration phase as a function of Re_{peak} as defined by (4.4). The plot is in log–log scale. The collapse of $\bar{u}_{F,peak}$ with Re_{peak} provides support for the difference in peak velocity for the different geometrical settings.

estimates are crude, but they provide qualitative support for the observed differences in peak velocity between the large- and small-release planar, and cylindrical currents.

The rapid increase in front velocity is to be expected, but the slight decrease before reaching a near constant value requires further investigation. A close look at the front during the acceleration phase is shown in figure 7, where, at several time instances, the front marked by the contour of span-averaged $\tilde{\rho} = 0.5$ is plotted along with span-averaged spanwise vorticity contours for the three-dimensional small-release planar case at $Re = 8950$. The results for all other cases are qualitatively similar. At around $\tilde{t} = 0.8$, the head of the current, as indicated by the $\tilde{\rho} = 0.5$ contour begins to lift up. Correspondingly, a local peak in spanwise vorticity begins to develop (not yet visible in the plot) indicating an incipient roll-up process. The roll-up process intensifies until $\tilde{t} \approx 2.5$, which corresponds to about $\bar{x}_F - \bar{x}_0 \approx 1$ when the front velocity levels off to a constant value (see figure 6). The decrease in front velocity following the peak clearly occurs alongside the roll-up of the interface between the advancing heavy and the retreating light fluid. Similar findings were reported by Härtel *et al.* (1999) for the case of slip surfaces, indicating that the bottom boundary layer plays no role in this process.

Simple arguments based on gravitational free fall starting from rest can be made to obtain a scale estimate for the dimensional acceleration time to peak velocity as $t_{peak} \approx u_{F,peak}/g'$. The scale for the front location at peak velocity can correspondingly be estimated as $x_{peak} - x_0 \propto H$. The computational results are in agreement with these simple scale estimates.

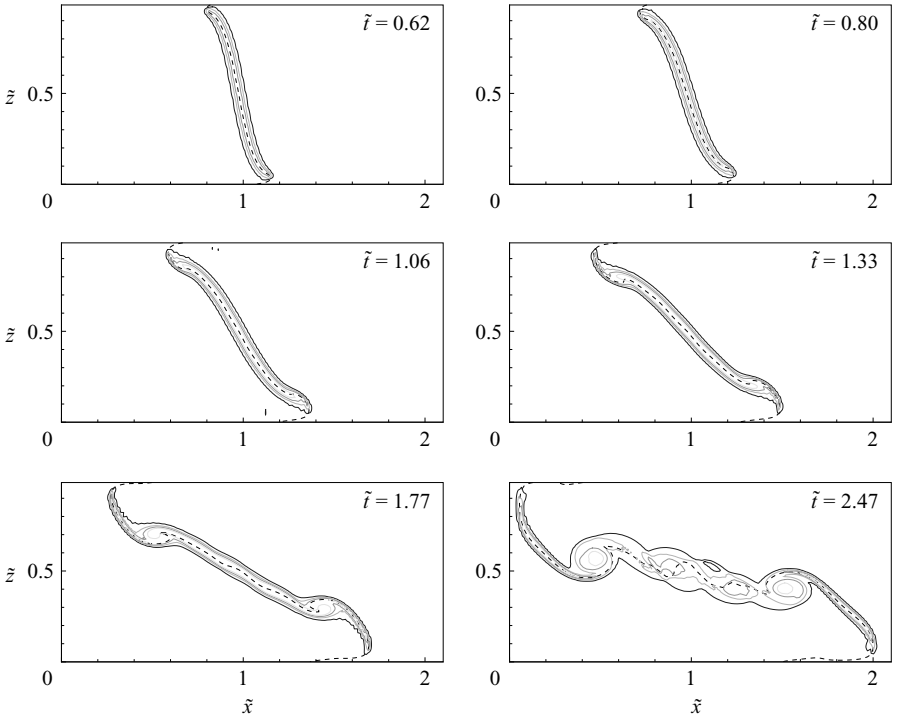

FIGURE 7. Flow evolution during the acceleration phase for the three-dimensional small-release planar current for $Re = 8950$. The dashed line shows the interface between the heavy and light fluids visualized by the span-averaged density contour $\tilde{\rho} = 0.5$. Solid lines represent contours of span-averaged spanwise vorticity. The front accelerates from rest and reaches the peak velocity at $\tilde{t} \approx 1$ (see also insets in figures 5 and 6). At this time, the roll-up of the interface begins and continues to develop until $\tilde{t} = 2.5$ ($\overline{x}_F - \overline{x}_0 \approx 1$), when deceleration of the front ends, and a constant front velocity is reached.

4.2.2. *Slumping phase*

From the insets in figure 5, it can be observed that both the large- and small-release planar cases approach a near constant velocity after the acceleration phase. In the cylindrical currents, a period of near constant velocity is not observed. The velocity, however, shows a brief period of rather slower variation before exhibiting a more pronounced decay of $\tilde{t}^{-1/2}$ in the inertial phase (this can be better seen in figure 8). Here, we take the duration of slow variation to be the approximate slumping phase and obtain a mean value for the average slumping phase velocity.

The near constant velocity of the slumping phase for the different cases considered herein is shown in table 2 along with previously reported results from experiments and numerical simulations. We observe from our simulations that the front velocity in the slumping phase remains the same for both the large- and small-release planar cases, i.e. the constant velocity is independent of the released volume. It is, however, dependent on the planar *vs.* cylindrical nature of the current and also shows a Reynolds-number dependence, over the range considered. Furthermore, from the insets in figure 5, it can be observed that the front velocity in the slumping phase is predicted well by two-dimensional approximations. Necker *et al.* (2002) reported similar results in the context of small-release planar particulate gravity currents. Here, we extend this analysis to large-release planar currents and cylindrical currents.

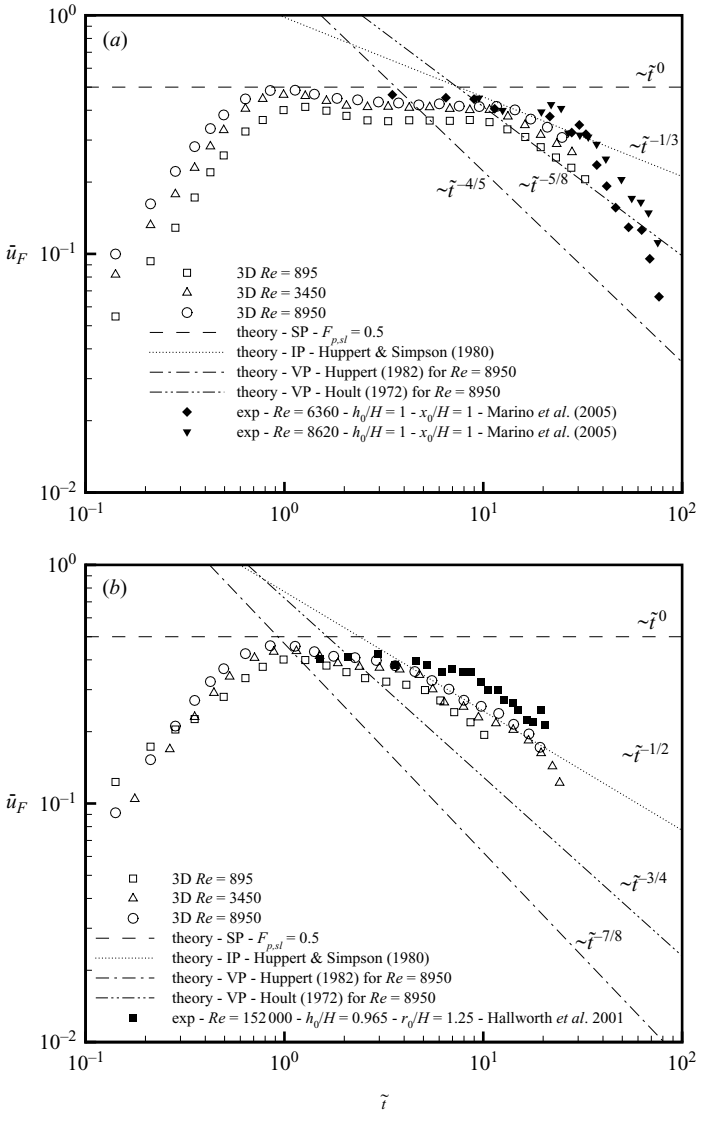

FIGURE 8. (*a*) Time evolution of the front velocity for planar currents with small release from three-dimensional simulations. The plot also includes experimental data from two of the lower *Re* experiments from Marino *et al.* (2005) with $\tilde{x}_0 = 1$ and $\tilde{h}_0 = 1$. Included also are the theoretical predictions for all the phases of spreading. The viscous phase predictions are for $Re = 8950$, $\tilde{r}_0 = 1$ and $\tilde{h}_0 = 1$. (*b*) Time evolution of the front velocity for cylindrical currents from three-dimensional simulations. The plot also includes experimental data from experiment S2 by Hallworth *et al.* (2001) with $\tilde{r}_0 = 1.25$ and $\tilde{h}_0 = 0.965$, and the theoretical predictions for all the phases of spreading. For this case, the planar case slumping phase theory prediction is used. The viscous phase predictions are for $Re = 8950$, $\tilde{r}_0 = 1$ and $\tilde{h}_0 = 1$.

The large- *vs.* small-release planar cases examine two basic effects of the aspect ratio (length over height) of the release, which varied from 8.5 for the large release to 1 for the small release, on the front velocity. The first is the effect on the value of the front velocity; the second is the duration of the constant velocity or slumping phase. Based on the similarity in the behaviour of the current front velocity during

Reference	*Re*	Planar large	Planar small	Cylindrical
Present work three-dimensional	895	0.361	0.361	0.318
Present work three-dimensional	3450	0.407	0.407	0.368
Present work three-dimensional	8950	0.421	0.421	0.408
Huppert & Simpson (1980)*		0.445		
Huppert & Simpson (1980) Exp. 5	25 900			0.402
Rottman & Simpson (1983)	9900–56 000		0.45	
Bonnecaze *et al.* (1995)	33 950			0.42
Härtel *et al.* (2000*b*) three-dimensional	3450	0.402		
Härtel *et al.* (2000*b*) two-dimensional	~10 900	0.429		
Necker *et al.* (2002) three-dimensional†	6325		0.409	
Shin *et al.* (2004)	1000 <	0.45		
Marino *et al.* (2005)	2790–133 000		0.45	
Hallworth *et al.* (2001)	152 000			0.42

TABLE 2. Mean front velocity, $\overline{u}_F$, in the slumping phase, with results for the present work from three-dimensional simulations. For comparison, previously published data is also presented. Data by Härtel *et al.* (2000*b*) and Necker *et al.* (2002) are from highly-resolved numerical simulations, and data by Huppert & Simpson (1980), Rottman & Simpson (1983), Shin *et al.* (2004), Marino *et al.* (2005) and Hallworth *et al.* (2001) are from laboratory experiments. For the cylindrical currents average values during the period of slow variation are reported, which are representative of the mean velocity during the slumping phase.
*Based on (3.3) with $\tilde{h}_F = 1/2$.
†Necker *et al.* (2002) report the front location for particulate gravity currents and also a case with zero particle settling velocity, which was used here.

the acceleration and the slumping phases, it can be concluded that the aspect ratio does not affect significantly the value of the front velocity during these two phases of spreading, despite the currents looking structurally very different owing to the nature of the release.

The aspect ratio has an effect, however, on the duration of the slumping phase. In the large-release cases, the constant velocity phase persists until the end of the simulation for the larger two *Re*. For the lower *Re*, viscous effects reduce the front velocity for $\tilde{t} > 10$. In the small-release cases, however, the constant velocity slumping phase extends over only a finite period for all the *Re*. Figure 8 presents the front velocity for the three-dimensional finite-volume release simulations, together with the scaling laws presented in the theory section. Figure 8(*a*) presents the results for the small-release planar case for the three *Re* considered, and figure 8(*b*) presents the results for the cylindrical case for the three *Re* considered. For comparison, this figure also includes experimental data from Marino *et al.* (2005) for the planar case at $Re = 6360$ and 8620 with $\overline{x}_0 = 1$ and $\overline{h}_0 = 1$, and from Hallworth *et al.* (2001) for the cylindrical case at $Re = 1.52 \times 10^5$, $\overline{r}_0 = 1.25$ and $\overline{h}_0 = 0.965$. In this last case, the comparison is not totally fair because the initial condition geometric parameters $\overline{r}_0$ and $\overline{h}_0$ are not exactly 1. Nevertheless, the agreement of our numerical results with the experimental data is good for both cases. Further comparison with more experiments is presented in the following sections.

From figure 8(*a*), it can be estimated that in the small-release planar case at $Re = 8950$, the constant-velocity phase is observed over $3 < \tilde{t} < 12$. The corresponding front location interval is $1 < \overline{x}_F - \overline{x}_0 < 5$ (5 lock lengths). During this period, the dimensionless height of the current at the head remains nearly constant at around 0.4

(see figure 3), which is in very good agreement with the experimental results of Marino *et al.* (2005). This indeed is also the maximum height of the current, and it continues to decrease upstream of the head. For the cylindrical case, it can be estimated from figure 8(*b*) that for $Re = 8950$ the nearly constant-velocity phase is observed over $2 < \tilde{t} < 4.5$. This corresponds to the front location interval $0.4 < \bar{r}_F - \bar{r}_0 < 1.7$ (1.7 lock radii). The predicted value of the front velocity for the larger Re simulation is 0.408, which is only about 3% lower than the value of Hallworth *et al.* (2001) at $Re = 152\,000$ (see table 2).

The dimensionless front velocity (or the Froude number) of the planar currents is substantially lower than 1/2, the value predicted by the hydraulic theories for full-depth release. This result is consistent with the numerical predictions of Härtel *et al.* (2000*b*) and the experimental observation of Shin *et al.* (2004) that the currents in their constant-velocity phase are consistently slower than the theoretical prediction by as much as 10% (see table 2). In particular, for the full-depth release, the Shin *et al.* (2004) experimental result yielded a Froude number of about 0.45 (see their figure 14 for $D/H = 1$). Similar results were reported by Rottman & Simpson (1983) and Marino *et al.* (2005) for the constant-velocity phase of finite volume releases (see table 2). Shin *et al.* (2004) conjectured that the deviation was primarily due to drag at the bottom wall. The effect of bottom friction was investigated by Härtel *et al.* (2000*b*).

4.2.3. *Inertial and viscous phases*

From figure 8(*a*), it can be observed that the small-release planar currents for the lower two Re depart from the constant-velocity phase at $\tilde{t} \approx 12$, after they have travelled about 4 lock lengths ($\bar{x}_F \approx 5$) for $Re = 895$ and about 5 lock lengths ($\bar{x}_F \approx 6$) for $Re = 3450$. After the transition, the front velocity follows a decaying law with a slope in good agreement to the viscous phase predictions presented in the theory section. For the case of the small-release planar current with $Re = 8950$, the front velocity departs from the constant-velocity phase at $\tilde{t} \approx 12$ after the current has travelled about 5 lock lengths ($\bar{x}_F \approx 6$). The front velocity follows the inertial phase scaling by Huppert & Simpson (1980) with good agreement until $\tilde{t} \approx 17.3$ ($\bar{x}_F \approx 8$), and after this time, it departs from the inertial phase scaling and falls off more rapidly following the viscous phase scaling laws. It can also be observed from this figure that the quantitative prediction of the viscous phase scaling laws is poor. Figure 8(*a*) includes the viscous phase predictions for $Re = 8950$ and it can be observed that both predictions by Hoult (1972) and Huppert (1982) underestimate the corresponding numerical result.

For the cylindrical current, the situation is similar. From figure 8(*b*), it can be observed that the current for the lower $Re = 895$ leaves the nearly constant velocity phase at $\tilde{t} \approx 5$ after it has travelled about 1.6 lock radii ($\bar{r}_F \approx 2.6$). After this time, the front velocity falls off rapidly with a slope in agreement with the viscous phase theoretical predictions. For the cases of the larger two Re, the front velocity leaves the nearly constant velocity phase at $\tilde{t} \approx 4.5$ ($\bar{r}_F \approx 2.7$) and follows the inertial phase prediction by Huppert & Simpson (1980) with good agreement up to $\tilde{t} \approx 17$ ($\bar{r}_F \approx 5.7$). At this time, the front velocity leaves the inertial phase and enters a phase of faster decaying. The viscous scaling laws by Hoult (1972) and Huppert (1982) for $Re = 8950$ are included in figure 8(*b*). Again, the viscous scaling laws underpredict the simulation results.

4.3. *Transition between phases of spreading*

The transition point between the different phases of spreading can be computed by matching front velocity from the corresponding scaling laws at the time of transition.

Reference	Re_{h_0}	$\tilde{h}_0$	$\tilde{x}_0$
Amy *et al.* (2005) Exp. A0-1	2220	1	1
Bonnecaze *et al.* (1993)	71 500	1	0.5
Marino *et al.* (2005) Exp. 1	2790	1	1
Marino *et al.* (2005) Exp. 2	6360	1	1
Marino *et al.* (2005) Exp. 3	8620	1	1
Marino *et al.* (2005) Exp. 4	15 500	1	1
Huppert & Simpson (1980) Exp. 1	15 700	1	2.62
Huppert & Simpson (1980) Exp. 2	28 000	1	2.66
Huppert & Simpson (1980) Exp. 7	16 200	0.34	0.89
Huppert & Simpson (1980) Exp. 9	42 500	0.33	0.87

TABLE 3. Experimental data used to revisit the scaling laws during the phases of spreading. Data for planar currents with finite volume release. Here, $Re_{h_0} = \sqrt{g' h_0^3}/\nu^2$.

Reference	Re_{h_0}	$\tilde{h}_0$	$\tilde{r}_0$
Bonnecaze *et al.* (1995)	34 000	1	1.89
Hallworth *et al.* (2001) Exp. S1	59 000	0.82	2
Hallworth *et al.* (2001) Exp. S2	152 000	0.965	1.25
Hallworth *et al.* (2001) Exp. S3	136 000	0.574	1.25
Hallworth *et al.* (2001) Exp. S7	201 000	0.565	1.25
Huppert & Simpson (1980) Exp. 1	18 400	1	4.67
Huppert & Simpson (1980) Exp. 3	26 000	1	3.24
Huppert & Simpson (1980) Exp. 4	19 000	1	3.24
Huppert & Simpson (1980) Exp. 5	26 000	1	1.47
Martin & Moyce (1952*b*)	4300	0.27	0.14

TABLE 4. Experimental data used to revisit the scaling laws during the phases of spreading. Data for cylindrical currents. Here, $Re_{h_0} = \sqrt{g' h_0^3}/\nu^2$.

Before matching, the first step is to obtain the prefactors for the different scaling laws to be applied in the slumping, inertial and viscous phases. A large collection of experimental data, covering a range of width and depth of release ($\overline{x}_0$ or $\overline{r}_0$ and $\overline{h}_0$) and Re, will be used. The experimental data used to this end are given in tables 3 and 4 for planar and cylindrical currents, respectively.

Figure 9 presents the front velocity as a function of time for the experimental data in tables 3 and 4 with open symbols. The geometric and Re effects have been scaled out appropriately in the different phases and the normalized front velocities are plotted in figure 9. Figures 9(*a*) and 9(*e*) present the velocity data scaled for the slumping phase for planar and cylindrical settings, respectively, figures 9(*b*) and 9(*f*) correspond to the inertial phase for planar and cylindrical settings, respectively, figures 9(*c*) and 9(*g*) correspond to the viscous phase based on the theory of Hoult (1972) for planar and cylindrical settings, respectively, and figures 9(*d*) and 9(*h*) correspond to the viscous phase based on the theory of Huppert (1982) for planar and cylindrical settings, respectively. Included in these figures also are the best fit to the data, where the theoretical power-law exponents are preserved and only the prefactor is optimized. In the slumping phase, from the best fit we obtain $F_{p,sl} = 0.45\,\overline{h}_0^{1/2}$ and $F_{c,sl} = 0.42\,\overline{h}_0^{1/2}$ for planar and cylindrical currents, respectively. Here, $F_{p,sl}$ and $F_{c,sl}$ denote the constant numerical value of $\overline{u}_F$ during the slumping phase for planar and cylindrical currents, respectively. In the inertial phase, the best fits yield $\xi_p = 1.47$ and $\xi_c = 1.23$ for planar

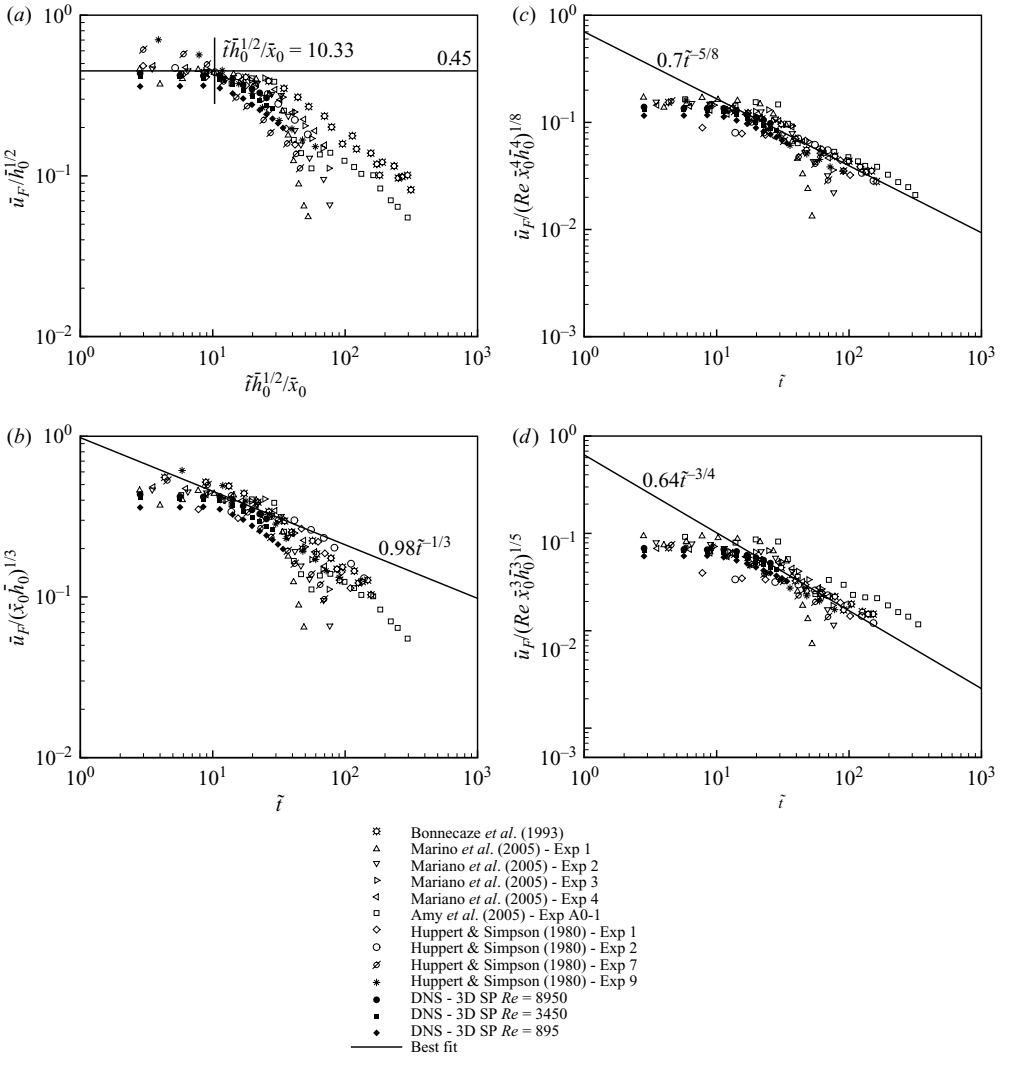

FIGURE 9(*a–d*). For caption see facing page.

and cylindrical currents, respectively (see (3.4) and (3.5)). In the viscous phase, the best fits yield $\xi_{pHt} = 1.87$ and $\xi_{cHt} = 2.6$ for the theory of Hoult (1972) (see (3.6) and (3.7)), and $\xi_{pHp} = 3.2$ and $\xi_{cHp} = 4.64$ for the theory of Huppert (1982) (see (3.8) and (3.9)). In figure 9, the data from our simulations are also included with solid symbols. Three things can be observed in these figures: (i) the agreement between numerical and experimental results is good; (ii) as *Re* increases, the numerical results approach the best fit; and (iii) the larger *Re* simulations seem to capture appropriately every phase of spreading for both geometrical configurations.

4.3.1. *Transition times for planar currents*

Matching the constant front velocity of the slumping phase, $F_{p,sl}$, with the front velocity of the inertial phase given in (3.4), the transition time from slumping to

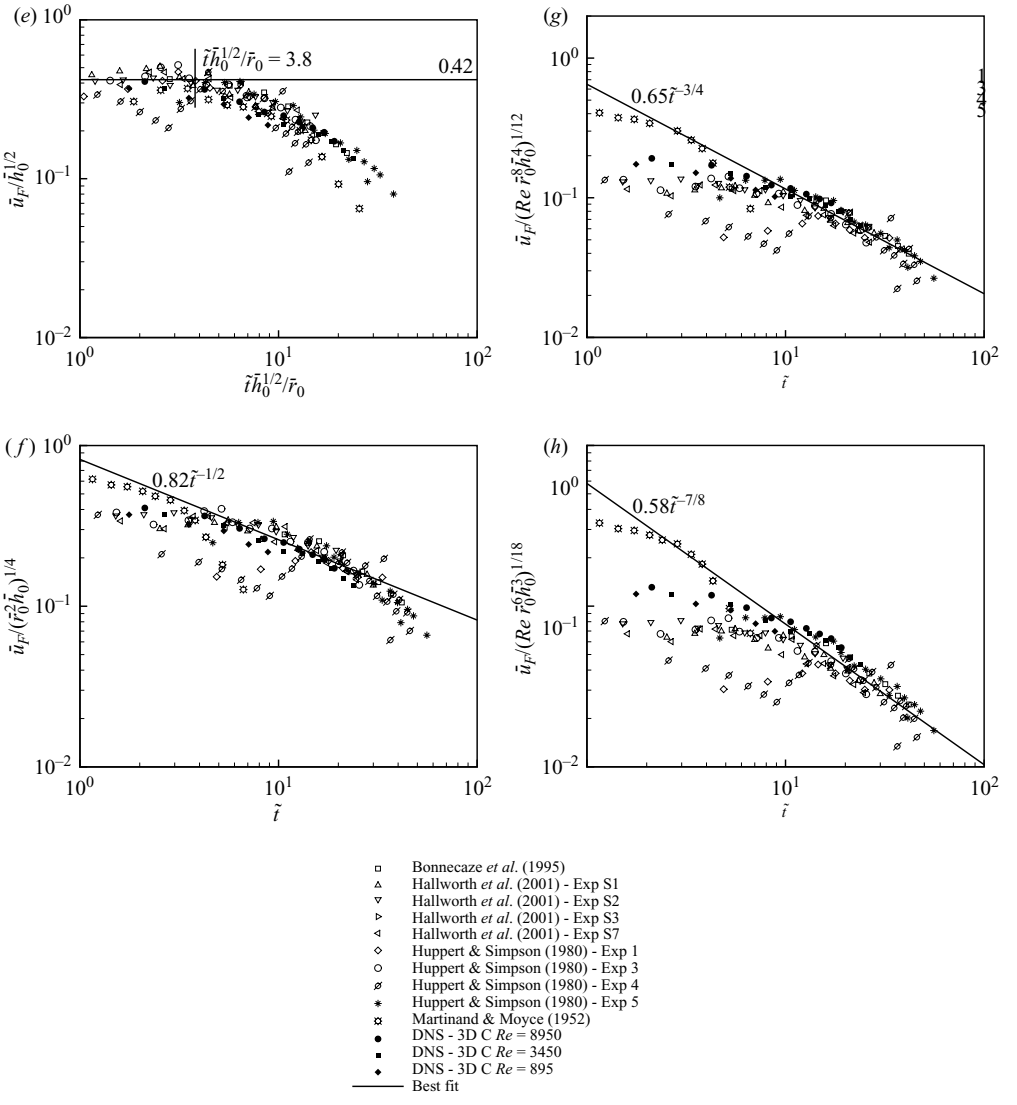

FIGURE 9. Front velocity during the slumping, inertial and viscous phases of spreading for planar and cylindrical currents. The plots include experimental data (open symbols) from tables 3 and 4, and the three-dimensional simulation results (solid symbols). The front velocity has been scaled according to the different scaling laws in order to remove the influence of initial condition and Re on $\overline{u}_F$. (*a*) Slumping phase for planar currents with small release; (*b*) inertial phase for planar currents with small release; (*c*) viscous phase for planar currents with small release for scaling law by Hoult (1972); (*d*) viscous phase for planar currents with small release for scaling law by Huppert (1982); (*e*) slumping phase for cylindrical currents; (*f*) inertial phase for cylindrical currents; (g) viscous phase for cylindrical currents for scaling law by Hoult (1972); (h) viscous phase for cylindrical currents for scaling law by Huppert (1982). Each plot also presents the best fit to the experimental data.

inertial phase, $\tilde{t}_{SI}$, of a planar current can be obtained as

$$\tilde{t}_{SI} = \left(\xi_p\right)^3 \frac{\overline{x}_0\,\overline{h}_0}{F_{p,sl}^3}\,. \tag{4.5}$$

Rescaling the transition time, we obtain

$$\frac{t_{SI}\sqrt{g' h_0}}{x_0} = \frac{\tilde{t}_{SI}\overline{h}_0^{1/2}}{\overline{x}_0} = \left(\tfrac{2}{3}\,\xi_p\right)^3 \left(\frac{F_{p,sl}}{\overline{h}_0^{1/2}}\right)^{-3}, \tag{4.6}$$

and using the best-fit results presented above, we obtain $\tilde{t}_{SI}\overline{h}_0^{1/2}/\overline{x}_0 = 10.33$. This predicted transition time is demarcated in figure 9(*a*) and captures well the time of departure from the constant-velocity phase for the experimental data.

The computational data present some Reynolds-number dependence, as can be confirmed in figure 8(*a*). The values of $F_{p,sl}/\overline{h}_0^{1/2}$ for the present simulations at $Re = 895$, 3450 and 8950 are 0.361, 0.407 and 0.421, respectively (table 2). Based on these values, the slumping to inertial phase transition times can be estimated from (4.5) as $\tilde{t}_{SI} = 20.0$, 14.0 and 12.6, for the three different Re cases. The slumping to inertial phase transition time identified in figure 8(*a*) for the higher $Re = 8950$ simulation is in good agreement with the prediction. With further increase in Re, the transition time can be expected to approach the asymptotic value of about 10.33. At the lower two Reynolds numbers, departure from the constant-velocity slumping phase occurs earlier and, as we will discuss below, this is due to direct transition from the slumping to the viscous phase.

The location at which transition between the slumping and inertial phases occurs can now be estimated as $x_{SI}/x_0 \approx u_F\, t_{SI}/x_0 = (2\,\xi_p/3)^3 (F_{p,sl}/\overline{h}_0^{1/2})^{-2}$. Again, using the best-fit values, we can obtain the following estimate: $x_{SI}/x_0 = 4.65$, which is lower than the accepted predicted value of x_{SI}/x_0 between 6 and 10 (Rottman & Simpson 1983; Metha *et al.* 2002; Marino *et al.* 2005). Note that the actual current velocity over a substantial portion of the acceleration phase is higher than the constant slumping phase velocity. This difference can partly explain the underestimation of transition location by the best-fit slumping phase velocity.

We now examine the possibility of direct transition from the slumping to the viscous phase by matching the constant velocity of the front in the slumping phase, $F_{p,sl}$, with the front velocity of the viscous phase given in (3.6) or (3.8). Depending on the viscous phase scaling employed, two different estimates for this transition time, $\tilde{t}_{SV}$, can be obtained as

$$\tilde{t}_{SVHt} = \left(\tfrac{3}{8}\xi_{pHt}\right)^{8/5} \frac{\left(\overline{x}_0\,\overline{h}_0\right)^{4/5}}{F_{p,sl}^{8/5}} Re^{1/5}, \tag{4.7}$$

$$\tilde{t}_{SVHp} = \left(\tfrac{1}{5}\xi_{pHp}\right)^{5/4} \frac{\left(\overline{x}_0\,\overline{h}_0\right)^{3/4}}{F_{p,sl}^{5/4}} Re^{1/4}. \tag{4.8}$$

For the present full-depth small-release planar currents ($\overline{h}_0 = \overline{x}_0 = 1$), using the best estimates for ξ_{pHt} and ξ_{pHp} and the values of $F_{p,sl}$ from table 2, we obtain $\tilde{t}_{SVHt} = 11.3$, 12.2 and 14.0, and $\tilde{t}_{SVHp} = 11.2$, 12.5 and 16.4, at $Re = 895$, 3450 and 8950, respectively.

At $Re = 895$, the predicted values for $\tilde{t}_{SV}$ by both theories are lower than the prediction for $\tilde{t}_{SI}$, which indicates that, in this case, the flow transitions directly from the slumping to the viscous phase without entering the inertial phase. From figure 8(*a*), it can be estimated that the current leaves the constant-velocity phase at $\tilde{t} \approx 12$, which is in good agreement with the predicted values of $\tilde{t}_{SV}$. The situation is similar for the intermediate $Re = 3450$ case, for which the predicted values of $\tilde{t}_{SV}$ are lower than $\tilde{t}_{SI}$, and as a result, this current can also be expected to transition directly

from the slumping to the viscous phase. The proximity of predicted $\tilde{t}_{SI}$ and $\tilde{t}_{SV}$ for this case suggests that this current is in the critical range of Re for an inertial phase to develop. For the case of $Re = 8950$, $\tilde{t}_{SV}$ is predicted to be larger than $\tilde{t}_{SI}$, which indicates that the flow is entering the inertial phase. From figure 8(*a*), the transition time from slumping to inertial phase for this Re can be estimated to occur at $\tilde{t} \approx 12$, which is in good agreement with the predicted $\tilde{t}_{SI} = 12.6$.

The transition time from the inertial to the viscous phase can be estimated by matching the front velocity from (3.4) with (3.6) or (3.8) as

$$\tilde{t}_{IVHt} = \left(\frac{3\,\xi_{pHt}/8}{2\,\xi_p/3}\right)^{24/7} (\overline{x}_0\,\overline{h}_0)^{4/7} Re^{3/7}, \tag{4.9}$$

$$\tilde{t}_{IVHp} = \left(\frac{\xi_{pHp}/5}{2\,\xi_p/3}\right)^{15/7} (\overline{x}_0\,\overline{h}_0)^{4/7} Re^{3/7}. \tag{4.10}$$

Using the best estimates of ξ_p, ξ_{pHt} and ξ_{pHp}, the prefactors in (4.9) and (4.10) can be obtained as 0.32 and 0.4, respectively. Except for this difference in prefactor, both the theories predict the same power-law behaviour. The predicted transition times for the $Re = 8950$ case are $\tilde{t}_{IVHt} = 15.7$ and $\tilde{t}_{IVHp} = 19.8$. From figure 8(*a*) it can be observed that the current leaves the inertial phase scaling at $\tilde{t} \approx 17.3$ ($\overline{x}_F \approx 8.1$) which is in good agreement with these predictions.

The slumping to inertial phase transition time, $\tilde{t}_{SI}$ in (4.5), has a weak Reynolds-number dependence through $F_{p,sl}$ and becomes Reynolds-number independent only at large Re. In contrast, $\tilde{t}_{SV}$ will continue to increase with Re. Thus, at lower Re, a direct transition from slumping to viscous phase occurs. However, at sufficiently large Re, $\tilde{t}_{SV}$ will become larger than $\tilde{t}_{SI}$ and a slumping to inertial phase transition will occur before eventual transition to the viscous phase, which is what we observe at $Re = 8950$. Matching (4.5) with (4.7) or (4.8) it can be estimated that the critical Re for the inertial phase to exist is

$$Re_{crHt} = \left(\frac{2\,\xi_p/3}{F_{p,sl}}\right)^{15} \left(\frac{F_{p,sl}}{3\,\xi_{pHt}/8}\right)^{8} \overline{x}_0\overline{h}_0 \qquad \text{for Hoult (1972)}, \tag{4.11}$$

$$Re_{crHp} = \left(\frac{2\xi_p/3}{F_{p,sl}}\right)^{12} \left(\frac{F_{p,sl}}{\xi_{pHp}/5}\right)^{5} \overline{x}_0\overline{h}_0 \qquad \text{for Huppert (1982)}. \tag{4.12}$$

Assuming the best fit values, we obtain $Re_{crHt} = 3400\,\overline{x}_0\,\overline{h}_0$ and $Re_{crHp} = 2000\,\overline{x}_0\,\overline{h}_0$. For $Re > Re_{cr}$ there will be an inertial phase, whereas for lower Re, the current will transition directly from slumping to viscous phase without an inertial phase. The present numerical results are in reasonable agreement with this prediction of Re_{cr}.

4.3.2. *Transition times for cylindrical currents*

The transition times between the different phases in a cylindrical current can be estimated in an analogous way. The transition time from slumping to inertial phase can be predicted by matching the constant velocity during the slumping phase, $F_{c,sl}$, with the inertial phase velocity scaling given in (3.5) as

$$\tilde{t}_{SI} = \left(\frac{\pi^{1/4}}{2}\xi_c\right)^2 \frac{\overline{r}_0\,\overline{h}_0^{1/2}}{F_{c,sl}^2}. \tag{4.13}$$

Rescaling the transition time we obtain

$$\frac{t_{SI}\sqrt{g'h_0}}{r_0} = \frac{\tilde{t}_{SI}\bar{h}_0^{1/2}}{\bar{r}_0} = \left(\frac{\pi^{1/4}}{2}\xi_c\right)^2 \left(\frac{F_{c,sl}}{\bar{h}_0^{1/2}}\right)^{-2}, \tag{4.14}$$

and using the best-fit results presented above, we obtain $\tilde{t}_{SI}\bar{h}_0^{1/2}/\bar{r}_0 = 3.8$. This predicted transition time is demarcated in figure 9(*e*) and it is in good agreement with the experimental data.

As with the planar case, Reynolds-number independence can be expected only at large *Re*. As can be seen in table 2 the values of $F_{p,sl}/\bar{h}_0^{1/2}$ for the present simulations at $Re = 895$, 3450 and 8950 are 0.318, 0.368 and 0.408, respectively, giving slumping to inertial phase transition times from (4.13) as $\tilde{t}_{SI} = 6.6$, 4.9 and 4.0, respectively. The slumping to inertial phase transition times identified in figure 8(*b*) for the higher two *Re* cases are in good agreement with the above prediction. At the lower *Re*, departure from the constant velocity slumping phase occurs earlier owing to direct transition from slumping to viscous phase.

The location at which transition between the slumping and inertial phases occurs can now be estimated as $r_{SI}/r_0 \approx u_F\, t_{SI}/r_0 = (\pi^{1/4}\xi_c/2)^2(F_{c,sl}/\bar{h}_0^{1/2})^{-1}$. Again, using the best fit values, we can obtain the estimate $r_{SI}/r_0 = 1.6$, which is lower than the corresponding experimental observation of $r_{SI}/r_0 \approx 3.0$ for $h_0/H = 1$ (Hallworth *et al.* 1996).

Slumping to viscous phase transition for the cylindrical current can be investigated by matching the constant front velocity of the slumping phase with the velocity scaling in the viscous phase given in (3.7) or (3.9). The resulting expressions for the transition time are

$$\tilde{t}_{SVHt} = \left(\tfrac{1}{4}\xi_{cHt}\right)^{4/3} \frac{\left(\bar{r}_0^2\,\bar{h}_0\right)^{4/9}}{F_{c,sl}^{4/3}} Re^{1/9}, \tag{4.15}$$

$$\tilde{t}_{SVHp} = \left(\tfrac{1}{8}\xi_{cHp}\right)^{8/7} \frac{\left(\bar{r}_0^2\,\bar{h}_0\right)^{3/7}}{F_{c,sl}^{8/7}} Re^{1/7}. \tag{4.16}$$

For the present full-depth currents ($\bar{h}_0 = \bar{r}_0 = 1$), using the best estimates of ξ_{cHt} and ξ_{cHp}, and corresponding values of $F_{c,sl}$ from table 2, the transition times predicted by (4.15) and (4.16) are $\tilde{t}_{SVHt} = 5.5$, 5.3 and 5.2, and $\tilde{t}_{SVHp} = 5.2$, 5.4 and 5.5, at $Re = 895$, 3450 and 8950, respectively.

For the case of $Re = 895$, the estimated value of $\tilde{t}_{SI}$ is larger than the predictions for $\tilde{t}_{SV}$ by both theories, which indicates that this current transitions directly from the slumping phase to the viscous phase. It can be observed from figure 8(*b*) that the current departs the constant velocity phase for $\tilde{t} \approx 5$, which is in good agreement with the predictions above for $\tilde{t}_{SV}$. For the cases of $Re = 3450$ and $Re = 8950$, the predicted values of $\tilde{t}_{SV}$ are larger than the predicted values for $\tilde{t}_{SI}$, which suggests the presence of an inertial phase at these *Re*.

The transition time from inertial to viscous phase, $\tilde{t}_{IV}$, can be predicted by matching the front velocity from (3.5) with (3.7) or (3.9) as

$$\tilde{t}_{IVHt} = \left(\frac{\xi_{cHt}/4}{\pi^{1/4}\,\xi_c/2}\right)^4 \left(\bar{r}_0^2\,\bar{h}_0\right)^{1/3} Re^{1/3}, \tag{4.17}$$

$$\tilde{t}_{IVHp} = \left(\frac{\xi_{cHp}/8}{\pi^{1/4}\,\xi_c/2}\right)^{8/3} \left(\bar{r}_0^2\,\bar{h}_0\right)^{1/3} Re^{1/3}. \tag{4.18}$$

For the cylindrical currents, both theories also predict the same Re dependence. The predicted transition times using the best-fit values are $\tilde{t}_{IV} = 6$ and 8.3 for both theories at $Re = 3450$ and $Re = 8950$, respectively. From figure 8(*b*), it can be estimated that the currents leave the inertial-phase scaling at $\tilde{t} \approx 17$ for both Re. This time is larger than the theoretical prediction by a factor of 2. It must be cautioned that the above estimates are based on an average constant velocity during the slumping phase. However, the actual front velocity slowly varies during the slumping phase.

Matching (4.13) with (4.15) or (4.16), the critical Re for the inertial phase to exist can be estimated as

$$Re_{crHt} = \left(\frac{\pi^{1/4}\,\xi_c/2}{F_{c,sl}}\right)^{18} \left(\frac{F_{c,sl}}{\xi_{cHt}/4}\right)^{12} \bar{r}_0 \bar{h}_0^{1/2} \quad \text{for Hoult (1972)}, \tag{4.19}$$

$$Re_{crHp} = \left(\frac{\pi^{1/4}\,\xi_c/2}{F_{c,sl}}\right)^{14} \left(\frac{F_{c,sl}}{\xi_{cHp}/8}\right)^{8} \bar{r}_0 \bar{h}_0^{1/2} \quad \text{for Huppert (1982)}. \tag{4.20}$$

With the best estimates of the constants, we obtain $Re_{crHt} = 880\,\bar{r}_0\,\bar{h}_0^{1/2}$ and $Re_{crHp} = 870\,\bar{r}_0\,\bar{h}_0^{1/2}$. For $Re > Re_{cr}$, there will be an inertial phase, whereas for lower Re, the current will transition directly from the slumping to the viscous phase without an inertial phase. This prediction of Re_{cr} is also in good agreement with our numerical results since we observe the $Re = 895$ case to transition directly to the viscous phase, whereas the simulations for $Re = 3450$ and $Re = 8950$ present an inertial phase.

It must be emphasized that the above estimates of transition times are sensitive to the exact value of the prefactors used with the different scaling laws. For instance, if we were to use the original prefactors presented in § 3.2 for ξ_p, ξ_c, etc., the resulting estimate for the critical Reynolds number for the existence of the inertial phase is much larger and differs significantly from the experimental and computational observation.

4.4. *Three-dimensionality of the flow*

At the lowest Re considered ($Re = 895$), the planar current remains two-dimensional and the cylindrical current remains axisymmetric at all times. The three-dimensional disturbances introduced in the initial condition do not grow over time at this Re. At the higher two Re, however, instabilities grow over time and the flow eventually becomes three-dimensional, forming a well-defined pattern of lobes and clefts and a turbulent front and body. Differences between two-dimensional and three-dimensional simulations were reported by Cantero (2002) for saline currents and by Necker *et al.* (2002) in the context of planar particulate gravity currents. Here, we identify and explain the mechanisms behind the spurious time variation of the front velocity during the viscous phase in two-dimensional simulations.

During the acceleration phase, the three-dimensional disturbances have not grown to sufficient strength to change the evolution of the current. Therefore, the three-dimensional and two-dimensional simulations yield nearly identical results during the acceleration phase in all the cases considered. As seen in figure 7, near the end of the acceleration phase the interface is marked by the complete development of two-dimensional Kelvin–Helmholtz rolls (or toroidal rolls in case of cylindrical currents). During the slumping phase, these rolls rapidly undergo three-dimensional instability and a fully developed three-dimensional state quickly follows. The three-dimensionality of the current, however, does not have a strong influence on the speed of the current during the slumping phase. Some small variations can be seen in

the inset in figure 5 between the two-dimensional and three-dimensional simulation results, but the overall evolution of the current remains unaffected.

The three-dimensionality of the current becomes important during the inertial and viscous phases. Substantial differences can be observed between the two-dimensional and three-dimensional results at later times in the insets in figures 5(*b*) and 5(*c*). Importantly, the three-dimensional current moves faster than the two-dimensional approximation and this difference is observed both in the planar and cylindrical currents. This implies that the speed of actual currents, which are invariably three-dimensional, will be underestimated by two-dimensional models. The other significant observation is that, while the speed of the three-dimensional currents smoothly decrease with time, the two-dimensional currents present periods of strong acceleration and deceleration. This non-monotonic behaviour of the two-dimensional current is related to the presence of strong coherent vortices and their episodic interaction in the form of vortex pairing.

4.4.1. *Lobes, clefts and spanwise variation*

The front of the current does not advance forward as one fixed entity. The propagation of the front presents some variation along the span (or along the circumferential direction) owing to the formation of lobes and clefts (Simpson 1972). Figure 10(*a*) shows, for example, the flow at the front of the three-dimensional small-release planar current for $Re = 8950$ at $\tilde{t} = 21.2$. In this figure, the location of the front is visualized by a thick solid line contour of $\tilde{\rho} = 0.01$, the horizontal flow is visualized by vectors and the vertical flow is visualized by thin line contours (solid line contours correspond to positive vertical velocity and dashed line contours to negative vertical velocity). The horizontal flow tends to diverge from the centre of the lobes and to concentrate in the clefts. Also the near-bed flow moves upward in the clefts and downward in the lobes.

The three-dimensional lobe and cleft structure of the advancing front can be seen in figure 11, which shows the flow structure of the three-dimensional small-release planar current for $Re = 8950$ at $\tilde{t} = 21.2$. At this time, the current is in the viscous phase of spreading. In figure 11(*a*), the flow is visualized by a surface of constant density ($\tilde{\rho} = 0.05$), and figure 11(*b*) shows contours of span-averaged $\tilde{\rho}$. The spanwise variation in front propagation continues after the initial formation of lobes and clefts and, as a result, the number and location of lobes and clefts constantly rearrange along the front. For example, figure 10(*b*) shows a composite picture of the front plotted on the $(\tilde{x}, \tilde{y})$-plane (top view) with several equispaced time intervals superposed for the three-dimensional small-release planar current for $Re = 8950$. At the beginning (toward the left-hand end of the plot), the front is nearly flat, but small random disturbances introduced in the initial condition quickly develop into well-formed lobe and cleft structures. This figure illustrates the footprint of clefts on the horizontal $(\tilde{x}, \tilde{y})$-plane as they advance over time. A complex pattern is etched by the clefts as the front advances, with repeated merger of the clefts and splitting of the lobes. The locations of transition from acceleration to slumping, from slumping to inertial and from inertial to viscous phases are marked in the figure by dotted lines. The lobe and cleft dynamics for the other cases simulated is similar and not shown here.

The lobe and cleft structure of the front has been observed and well documented in several laboratory experiments (see for example Simpson 1972, 1997; Spicer & Havens 1987; García & Parker 1989). With increasing time, the instantaneous Reynolds of the flow, $Re_F = u_F h_H / \nu = Re\, \overline{u}_F \overline{h}_H$, decreases and this decrease in Re_F has the dominant influence on the increase in the length scale of the lobe and cleft pattern. Figure 10(*c*)

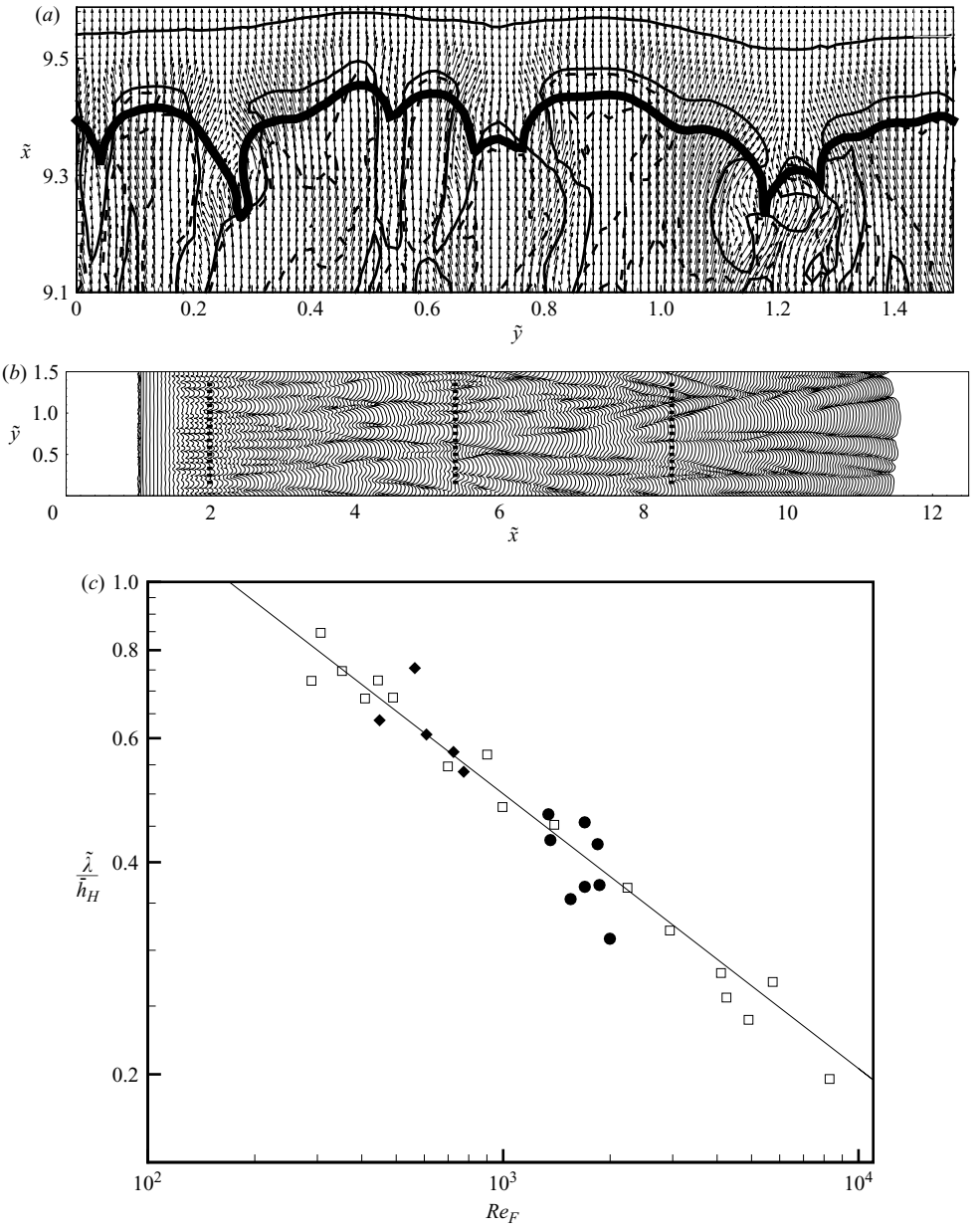

FIGURE 10. (*a*) Near-bed flow pattern at the front of the small-release gravity current for $Re = 8950$ for $\tilde{t} = 21.2$ when the front is located at $\tilde{x} \approx 9.5$. Vectors show the horizontal flow at $\tilde{z} = 0.03$. Thin line contours show vertical flow velocity at the same height, solid line for positive vertical velocity and dashed line for negative vertical velocity. The thick solid line indicates the front location visualized by a bottom density contour of $\tilde{\rho} = 0.01$. (*b*) Time evolution of lobe and cleft pattern in the three-dimensional small-release planar current for $Re = 8950$ visualized by contours of constant density ($\tilde{\rho} = 0.01$). The time separation between contours is $\Delta\tilde{t} = 0.014$. Dotted lines mark the transition locations between acceleration/slumping, slumping/inertial and inertial/viscous phases. (*c*) Lobe size as a function of local Reynolds number $Re_F = Re\,\bar{u}_F\,\bar{h}_H$. The figure includes our results from the three-dimensional small-release planar current for $Re = 3450$ (solid diamonds), $Re = 8950$ (solid circles), and from experimental data by Simpson (1972) (open squares). The line is the empirical prediction by Simpson (1972): $\tilde{\lambda}/\bar{h}_H = 7.4\,Re_F^{-0.39}$.

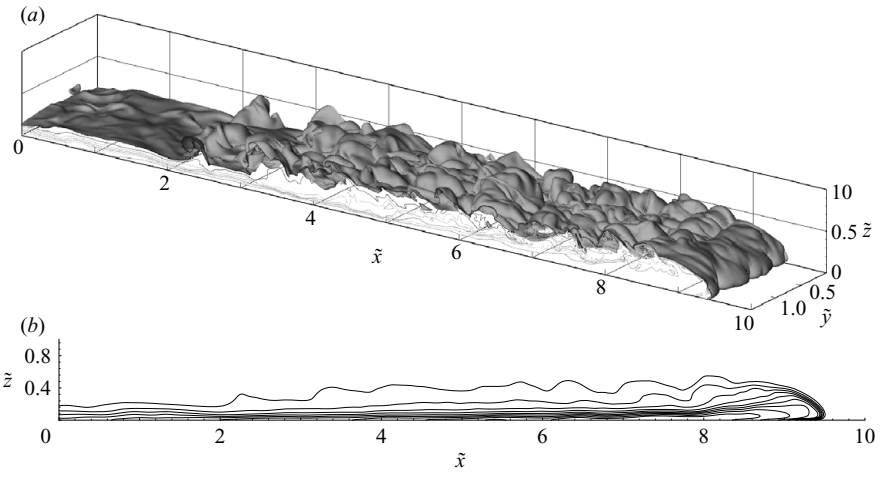

FIGURE 11. Flow structure of the three-dimensional small-release planar current for $Re = 8950$ at $\tilde{t} = 21.2$. (*a*) Isosurface of $\tilde{\rho} = 0.05$, and (*b*) contours of span-averaged $\tilde{\rho}$. At this time, the current is in the viscous phase of spreading and shows a complex state of three-dimensionality.

shows the normalized lobe size, $\tilde{\lambda}/\bar{h}_H$, as a function of Re_F for the three-dimensional small-release planar currents at $Re = 3450$ and $Re = 8950$. Also in the figure are the experimental data of Simpson (1972) and his empirical prediction $\tilde{\lambda}/\bar{h}_H = 7.4\, Re_F^{-0.39}$. The numerical results present very good agreement with the experimental data. This Re effect on the wavelength of the lobe and cleft pattern is in agreement with the results on the most unstable mode from the linear stability analysis of Härtel, Carlsson & Thunblom (2000*a*).

The non-uniform structure of the front is better illustrated in figure 12, where the front location $\tilde{x}_F$ is plotted as a function of the spanwise coordinate ($\tilde{y}$ for planar currents and θ for cylindrical currents). Only the three-dimensional highest $Re = 8950$ simulations are considered. Figure 12(*a*) shows the front location of the large-release planar current at $\tilde{t} \approx 7.6$, after the front has travelled approximately 3 dimensionless units from the lock ($\overline{x}_F = 11.5$). For the small-release planar current, figure 12(*b*) shows the front location at two different time instances, one at the earlier slumping phase ($\tilde{t} \approx 7$) when the front is located approximately at $\tilde{x} \approx 4$, and another one at a later time in the viscous phase ($\tilde{t} \approx 23$) after the front has travelled to $\tilde{x} \approx 10$. Figure 12(*c*) shows the front location for the cylindrical current during the slumping phase ($\tilde{t} \approx 3$) and during the viscous phase ($\tilde{t} \approx 18$) for only one quadrant of the complete computational domain.

The variation in the front location can also be measured in terms of the root mean square (r.m.s.) deviation in front location from the mean and is shown in table 5 for the two larger Re in the slumping and viscous phases for the different cases considered in figure 12. A comparison of the two different time instances shown in figure 12(*b*) shows that the r.m.s. fluctuation is larger in the viscous phase than in the slumping phase, both in the planar and cylindrical currents. Thus, not only does the size of lobes increase with time as indicated by figure 10(*c*), but also, with increasing time or diminishing local Re_F, these lobes become more prominent as indicated by these r.m.s. values. A comparison of the cylindrical and planar results shows that the cylindrical configuration presents a larger variation of front location.

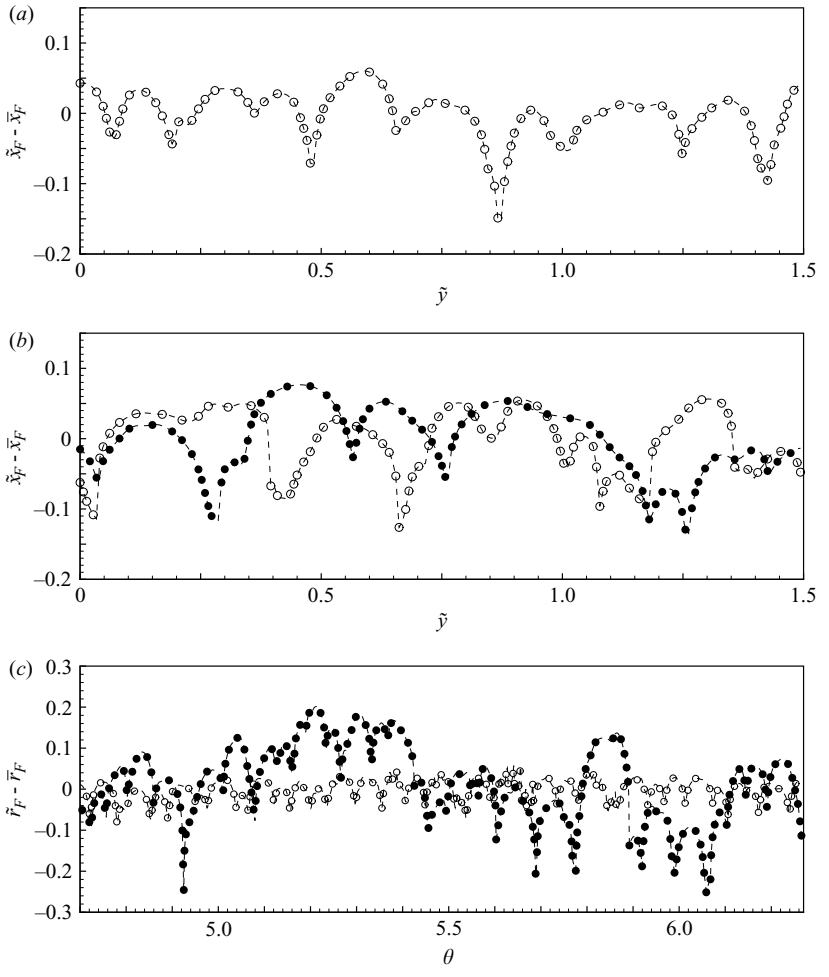

FIGURE 12. Spanwise (circumferential) variation of the front location for $Re = 8950$. (*a*) Front location for the three-dimensional large-release planar configuration at $\tilde{t} \approx 7.6$ ($\bar{x}_F \approx 11.5$). (*b*) Front location for the three-dimensional small-release planar current at two different time instances, one at the earlier slumping phase, $\tilde{t} \approx 7$, (open symbol) when the front is located approximately at $\tilde{x} \approx 4$, and another one at a later time in the viscous phase, $\tilde{t} \approx 23$, (solid symbols) after the front has travelled to $\tilde{x} \approx 10$. (*c*) Front location for the three-dimensional cylindrical current during the slumping phase, $\tilde{t} \approx 3$ (open symbol) and during the viscous phase $\tilde{t} \approx 18$ (solid symbol).

4.4.2. *Three-dimensionality of the current body*

The body of the current is much more complex and three-dimensional than is shown in figure 11. The undulations seen in the span-averaged contours (figure 11*b*) provide a clear indication of Kelvin–Helmholtz instability and the presence of a periodic train of rolled-up vortices. The imprint of these rolls can be seen in the three-dimensional density contour (figure 11*a*), where they appear to be bent, stretched, and eventually broken up into smaller-scale structures. These small structures can be observed in the body of the current behind the leading front, giving the appearance of a turbulent wake that eventually dissipates toward the tail of the current. Similar observations were made in cylindrical currents (Cantero *et al.* 2006) and will not be presented

	Re	Planar large	Planar small	Cylindrical
Slumping	3450	4.1×10^{-2} (8.2)	4.6×10^{-2} (7.5)	0.9×10^{-2} (3.1)
phase	8950	3.5×10^{-2} (7.6)	4.55×10^{-2} (7.1)	1.95×10^{-2} (3.0)
Viscous	3450	–	0.9×10^{-1} (24.7)	0.65×10^{-1} (19.7)
phase	8950	–	4.8×10^{-2} (22.8)	1.4×10^{-1} (17.7)

TABLE 5. Front location r.m.s. for selected times in slumping and viscous phases. The results are reported with the time from release between brackets: r.m.s. ($\tilde{t}$), to correlate these results with insets in figures 5(a), 5(b) and 5(c).

here in detail. The turbulent three-dimensional structure of the body of the current has been observed and well documented in numerous experiments (see for example Simpson & Britter 1979; García & Parker 1989; Alahyari & Longmire 1996; García & Parsons 1996; Simpson 1997; Parsons & García 1998; Thomas, Dalziel & Marino 2003).

The complex three-dimensional vortical structure of the wake is not entirely apparent in the density isosurface presented in figure 11(a). The corresponding isosurface of *swirling strength*, $\tilde{\lambda}_{ci}$, defined as the absolute value of the imaginary portion of the complex eigenvalues of the local velocity gradient tensor, is shown in figure 13. (The local velocity gradient tensor has three eigenvalues. If all three eigenvalues are real, then swirling strength is zero. If only one eigenvalue is real, then the other two are complex conjugates and there is local swirling motion.) As discussed in Zhou *et al.* (1999) and Chakraborty, Balachandar & Adrian (2005), the swirling strength provides a clean measure of the compact vortical structures of the flow as it picks out regions of intense vorticity, but discriminates against planar shear layers, where vorticity is balanced by strain rate. Thus, as can be seen from figure 13, the three-dimensional vortical structure of the high Re planar current is extracted well by $\tilde{\lambda}_{ci}$. At the time instance shown, the mean and r.m.s. values of dimensionless $\tilde{\lambda}_{ci}$ are 0.16 and 0.57, respectively. In figure 13(a), the isosurface of $\tilde{\lambda}_{ci} = 2.12$ is plotted and thus it captures intense vortical regions. The flow is dominated by inclined vortical structures and several hairpin vortices can be observed (indicated by arrows). These structures are similar to those observed in a turbulent wall layer, where the vortical structures are tilted from the wall in the flow direction. The gravity current shown in figure 13(a) flows to the right. In a frame of reference moving with the front, the flow within the current can be from right to left which explain the observed orientation of the vortical structures within the current. The net effect of the vortical structures on the concentration (density) field is seen in figure 11. The isosurface of swirling strength confirms what was observed earlier in the density isosurface, that is, the body of the current is far more three-dimensional than the head.

Also plotted in figures 13(b) and 13(c) are the contours of span-averaged swirling strength for the three-dimensional planar simulation and the swirling strength for the two-dimensional planar simulation at $Re = 8950$, respectively. The substantial difference between the three-dimensional evolution and the two-dimensional approximation is highlighted in this figure. At the instance shown, the signature of a sequence of Kelvin–Helmholtz vortices can be seen in the two-dimensional swirling strength at $\tilde{x} \approx 5.9$, 6.6, 7.7, 8.2 and 8.6. The span-averaged vortex signature in the three-dimensional simulation is not as well defined as in the two-dimensional simulation. The two-dimensional result shows several coherent

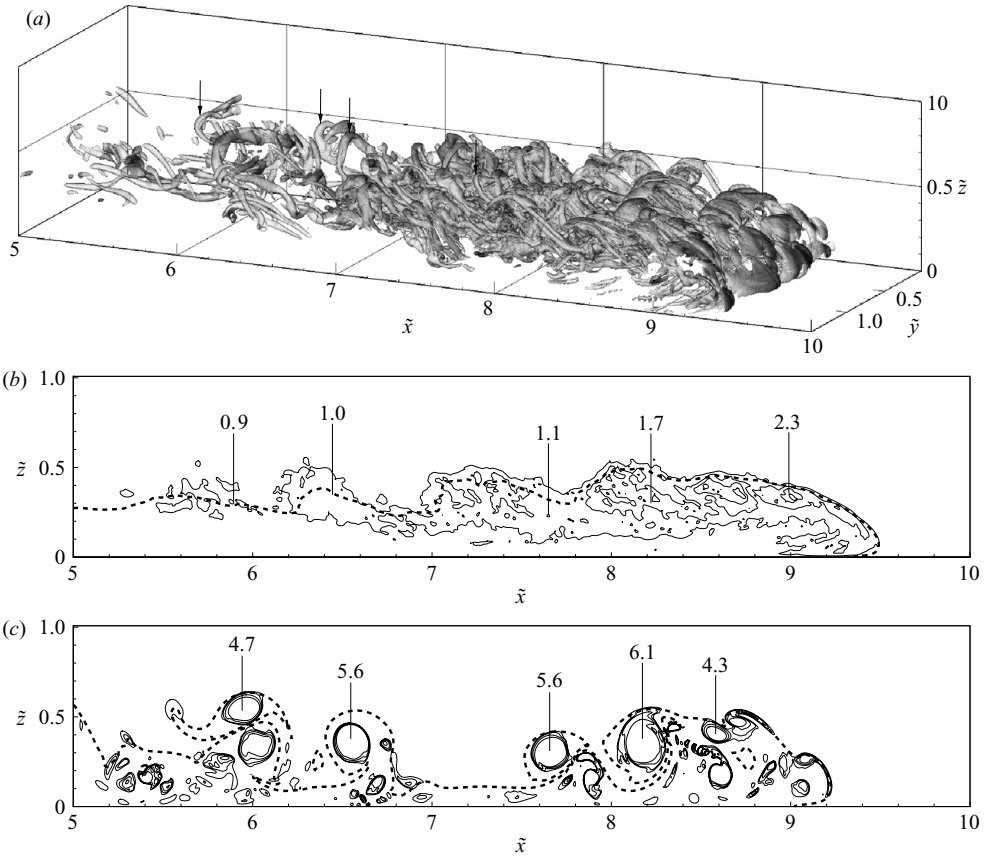

FIGURE 13. Contours of $\tilde{\lambda}_{ci}$ for the small-release planar current for $Re = 8950$ at $\tilde{t} = 21.2$. (*a*) Isosurface of $\tilde{\lambda}_{ci} = 2.12$ from the three-dimensional simulation; (*b*) contours of span-averaged $\tilde{\lambda}_{ci}$ from the three-dimensional simulation; (*c*) contours of $\tilde{\lambda}_{ci}$ from the two-dimensional simulation. In (*a*) several hairpin vortices are pointed with arrows to help their visualization. The dashed line in (*b*) and (*c*) represents the interface visualized by the contour of span-averaged density $\tilde{\rho} = 0.05$. In (*b*) and (*c*), the inset numbers indicate local values of span-averaged and two-dimensional $\tilde{\lambda}_{ci}$, respectively.

primary (counterclockwise rotating) vortices along the length of the current. Also present are secondary (clockwise rotating) vortices induced by the interaction of the primary vortices with the no-slip wall. In figure 13(*c*), the vortices are undergoing a complex interaction process of pairing and merging. Another striking difference between the three-dimensional and two-dimensional simulations is the strength of the rolled-up vortices, which are indicated in figure 13 by the inset numbers. In the two-dimensional approximation, the vortices just formed upstream of the head are two to three times stronger than their three-dimensional counterpart. Furthermore, as the vortices move upstream of the head, they lose their strength more rapidly in the three-dimensional simulation, whereas in the two-dimensional approximation, the coherence of the vortices is preserved and, therefore, their decay is not as strong. Also overlaid on figures 13(*b*) and 13(*c*) as a dashed line is the current interface plotted in terms of the span-averaged density contour of $\tilde{\rho} = 0.05$. The two-dimensional approximation shows large variation in the current height, which is clearly associated

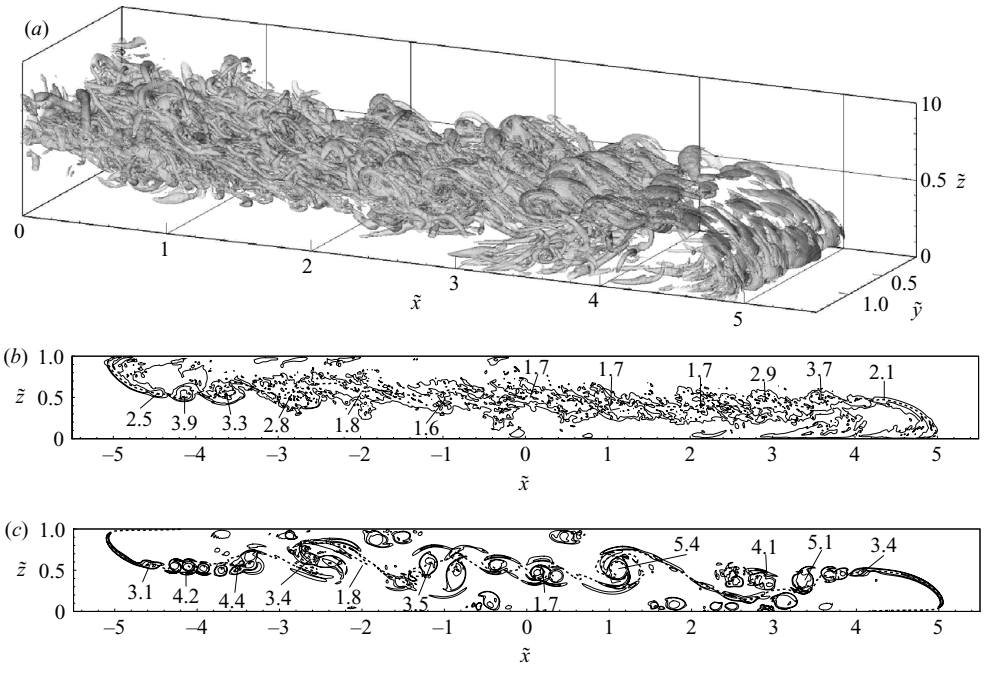

FIGURE 14. Contours of $\tilde{\lambda}_{ci}$ from the large-release planar current for $Re = 8950$ at $\tilde{t} = 12$. (*a*) Isosurface of $\tilde{\lambda}_{ci} = 2.12$ (shown only for $\tilde{x} > 0$) from the three-dimensional simulation; (*b*) contours of span-averaged $\tilde{\lambda}_{ci}$ from the three-dimensional simulation; (*c*) contours of $\tilde{\lambda}_{ci}$ from the two-dimensional simulation. The dashed line in (*b*) and (*c*) represents the interface visualized by the contour of span-averaged density $\tilde{\rho} = 0.5$. In (*b*) and (*c*), the inset numbers indicate local values of span-averaged and two-dimensional $\tilde{\lambda}_{ci}$, respectively.

with the presence of strong coherent vortices. The height variations are present even in the three-dimensional simulation (see also figures 3 and 4), but the undulations are much weaker.

4.4.3. *Three-dimensionality of the flow during the slumping phase*

We now address three-dimensionality of the current in the constant-velocity slumping phase. Figure 14(*a*) shows the isosurface of $\tilde{\lambda}_{ci} = 2.12$ for the $Re = 8950$ large-release planar current at $\tilde{t} = 12$. At this instance, the mean and r.m.s. values of $\tilde{\lambda}_{ci}$ are 0.28 and 0.74, respectively. Also shown in figures 14(*b*) and 14(*c*) are contours of $\tilde{\lambda}_{ci}$ from the span-averaged result of the three-dimensional and two-dimensional simulations, respectively. In the isosurface visualization, only the advancing front of the heavy fluid ($\tilde{x} \geqslant 0$) is shown. The vortical structure of the current is qualitatively very similar to that seen in figure 13 for the small-release planar case in the viscous phase. An important difference is that the rolled-up vortices are farther upstream of the front. At the instance shown, the vortices are generally at least 1 dimensionless unit upstream of the front, whereas in the viscous phase shown in figure 13, the vortices are much closer to the front. For instance, the dominant vortex at $\tilde{x} \approx 1$ is about 4 dimensionless units upstream of the front, whereas in figure 13, the dominant vortex is only 1 dimensionless unit upstream of the front. Differences between three-dimensional and two-dimensional results are still present in terms of stronger Kelvin–Helmholtz vortices. However, these vortex cores are farther upstream

of the front so they do not interact with it. Consequently, their influence on front velocity is not strong and the two-dimensional and three-dimensional fronts advance at about the same mean velocity.

As indicated in the insets in figure 5, only the average speeds of the two-dimensional and three-dimensional currents are the same in the slumping phase. Instantaneous location and velocity of the current fluctuates as the interface rolls up to form new vortices and as the older vortices interact. As can be seen at the instance shown in figure 14, the two-dimensional current has advanced slightly ahead of the three-dimensional current. A comparison of figure 14 in the slumping phase with figure 13 in the viscous phase shows, that in the slumping regime, the strong rolled-up vortices are located farther upstream of the front, whereas in the inertial and viscous phases they are closer to the front of the current. This, we believe, is the reason why three-dimensionality has a stronger influence on the propagation speed of the current in the viscous phase.

4.4.4. *Time variation*

It can be observed in the insets in figure 5 that the two-dimensional simulations present strong time variation in the mean front velocity during the viscous phase. This time variation is related to strong vortex interaction, which is absent in the three-dimensional simulations. In the two-dimensional approximation, the spanwise vortices remain coherent and exhibit strong interaction in terms of pairing and leap-frogging. Lack of three-dimensionality prevents vortex stretching and breakup, and therefore the rolled-up vortices maintain their strength and remain in the flow for a longer time, allowing them to interact strongly with each other. Figure 15 shows the mean front velocity in the two-dimensional small-release planar current for $Re = 8950$. A sequence of vortex pairing is shown as insets (*a*) to (*e*), each separated with a time interval of 0.71 time units. These times are also marked in the plot of front velocity to allow connection between the dynamics of vortex pairing in relation to the mean front velocity variation. In the insets, the front of the current is visualized by density contours. Solid lines represent $\tilde{\rho} < 0.3$ and dashed lines represent $\tilde{\rho} \geqslant 0.3$. Five vortical structures marked 1 to 5 can be identified in figure 15, inset (*a*). Vortices 1, 2, 4 and 5 rotate counter-clockwise, and vortex 3 rotates clockwise. The vortex pairing begins with the interaction of vortices 3 and 4, which elongates vortex 4 (see figure 15, inset (*b*)) giving space for the growth of vortex 3. Following the growth of vortex 3, the interaction of vortices 2 and 3 begins and, as a consequence, vortex 2 acts as a pump of heavy fluid at the expense of its own kinetic energy. The centre of mass of vortex 3 is raised and this results in an increase of its potential energy, which can be visualized in figure 15, inset (*c*). At this time the acceleration of the front begins. The acceleration of the front is driven by the enhanced potential energy of vortex 3, whose centre of mass moves down as the front advances (see figure 15, insets (*d*) and (*e*)).

The above sequence is just an example. Similar vortex interaction processes are responsible for other pronounced variations in the front velocity observed in figure 15. The details of vortex interaction subtly vary, but the interaction process remains qualitatively the same and is present in the cylindrical currents as well. Vortex interaction occurs in three-dimensional simulations as well; however, because of their reduced strength and coherence, the interactions are not nearly as powerful. Detailed investigation of the flow shows strong vortex interactions in the two-dimensional simulations, even in the constant velocity slumping phase. These interactions are

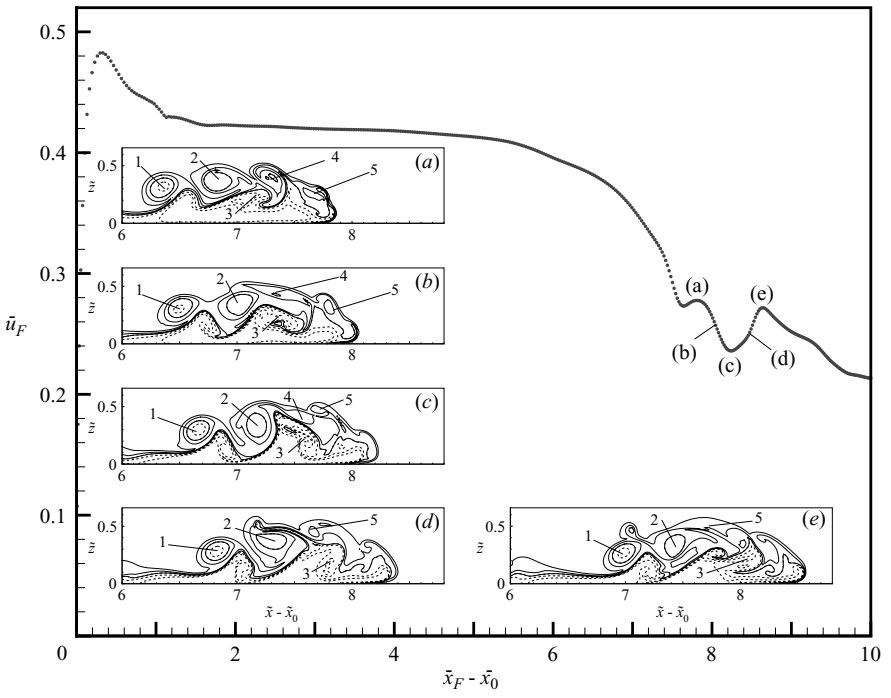

FIGURE 15. Vortex interaction in the two-dimensional small-release planar current for $Re = 8950$. The main figure shows the mean front velocity as a function of distance travelled by the front. The insets show the head of the current visualized by density contours. Five different time instances with time interval of 0.71 are shown, marked (*a*)–(*e*) in the main figure. Solid lines represent contours of $\tilde{\rho} < 0.3$ and dashed lines represent contours of $\tilde{\rho} \geqslant 0.3$. Five different individual vortex cores (billows) are shown in the different frames.

farther upstream of the front than in the viscous phase, and as a result the velocity variation in the slumping phase is less pronounced.

5. Summary and conclusions

In this work, we present highly resolved two-dimensional and three-dimensional simulations of gravity currents performed at $Re = 895$, 3450 and 8950. The particular choice of $Re = 3450$ corresponds to a Grashof number $Gr = 1.5 \times 10^6$, the dimensionless parameter used by Härtel *et al.* (2000*b*) in their planar current simulations. The other two Re correspond to $Gr = 10^5$ and $Gr = 10^7$. We consider both planar and cylindrical configurations, and in the planar currents we vary the volume of the heavy fluid released into the lighter ambient fluid. The simulations have been conducted with a de-aliased spectral code for the planar two-dimensional and three-dimensional configurations, and for the cylindrical three-dimensional configuration. A spectral multi-domain code has been used for the axisymmetric (two-dimensional cylindrical) configuration. These highly accurate numerical formulations allow the capture of all relevant length scales present in the flow.

The main objectives of the study are to examine the effect of the planar *vs.* the cylindrical nature of the current, the influence of the volume of release on the propagation of the front, the transition between phases, and the three-dimensionality of the flow during the various phases of spreading. The planform area of a planar

current increases linearly, whereas it does so quadratically for a cylindrical current, resulting in fundamental differences in the spreading rate. In all the cases, as the front accelerates from rest, the front velocity increases and reaches a maximum, after which the front velocity decreases somewhat before settling to a near constant value. The value of peak front velocity reached by the current increases with Re. Owing to the quadratic spreading, the intensity of the cylindrical current weakens more rapidly and, as a result, the peak velocity is lower than the planar counterpart for the same initial Re. This maximum is reached after the front has advanced about 0.3 height units regardless of the Re of the flow and the geometrical setting. This is, however, for the ideal case of infinite gate lift velocity, and some deviation may be expected in real experiments because of the finite time it takes to release the gate.

A close look at the interface between the heavy and light fluids shows that at about the time the front velocity peaks, the interface begins to roll up, and at about the time the roll up process saturates, the deceleration of the front ends and the constant velocity phase begins. In the constant velocity slumping phase of the planar currents, we observe the dimensionless height of the current to be lower than the theoretical prediction of 1/2 (Benjamin 1968; Shin *et al.* 2004) for energy-conserving currents. The corresponding constant dimensionless front velocity is also observed to be lower than 1/2. Based on the limited range of Re investigated in the present study, a crude estimation for the constant velocity for the planar currents at asymptotically large Re is about 0.44. This asymptotic value is lower than the theoretical prediction by both Benjamin (1968) and Shin *et al.* (2004), but is in reasonable agreement with previously reported data presented in table 2 and with the best fit to the experimental data presented in figure 9(*a*). Härtel *et al.* (1999) have considered the start-up stages of gravity currents with slip surfaces, and their results show the presence of a slight deceleration in the current speed past the peak value. Also, Härtel *et al.* (2000*b*) report slip surfaces front velocities to be lower than the theoretical prediction of 0.5 even at large Re. These cases show that the reduction in the front velocity occurs regardless of the existence of the bottom boundary layer. In the present simulations, in addition to energy loss to wall friction, part of the potential energy goes towards maintaining internal recirculation within the rolled-up vortices. Only the balance goes towards the kinetic energy of the advancing front. This partitioning of energy has not been accounted for in the existing theories. It can be conjectured that perhaps by accounting for internal fluid motion it may be possible to predict better the actual current height and velocity (see also Härtel *et al.* 2000*b*).

Over the entire computed time interval, the large-release planar currents for the larger two Re are not substantially affected by viscous effects and remain in the constant velocity slumping phase. The small-release planar and cylindrical currents remain in the slumping phase only for a finite time interval, and transition to the inertial or viscous phase. In the case of the planar currents, the nearly constant velocity of spreading during the slumping phase is not affected by the size of release.

The Re of the present planar small-release simulations are not adequate for an inertial phase to develop clearly. The transition is directly to the viscous phase for the lower two Re simulations, whereas the larger Re simulation enters the inertial phase for a brief period of time. In the case of the cylindrical currents, the larger two Re simulations present an inertial phase of spreading, whereas the lower Re simulation transitions from the slumping phase directly to the viscous phase. The transition times between phases can be estimated by matching velocity at the same time using the different scaling laws. We have revisited the prefactors in the slumping, inertial and viscous phase scaling laws in the light of previously reported experimental data. With

the revised scaling laws, we predict transition from the slumping to the inertial phase to occur at $t/T_0 \approx 10$ for planar currents and at $t/T_0 \approx 4$ for cylindrical currents, independently of the volume of release. Here, $T_0 = x_0/\sqrt{g' h_0}$ (or $T_0 = r_0/\sqrt{g' h_0}$). These predictions are in very good agreement with the experimental data and our experimental results.

For the present small-release planar configuration, it can be estimated that the Re must be greater than about $3400\,\bar{x}_0\,\bar{h}_0$ for the inertial phase to exist, and for the cylindrical configuration, the Re must be greater than about $880\,\bar{r}_0\,\bar{h}_0^{1/2}$.

The actual evolution of the front differs from simple theoretical prediction in several significant ways. The Kelvin–Helmholtz vortices formed at the interface strongly interact among themselves and with the bottom boundary in a complex chaotic manner. In response to vortex pairing, leap-frogging and other such interaction processes, the propagation of the front undergoes episodic rapid acceleration and deceleration. The vortex interaction is stronger in the case of two-dimensional (or axisymmetric) approximation, and as a result the undulations in front velocity are pronounced. The spanwise (or circumferential) coherence of the Kelvin–Helmholtz vortices is broken in three-dimensional simulations. In these cases, vortex interaction is substantially weaker and result in much weaker undulations in front velocity.

At the lowest Re of 895, in all the cases considered, the three-dimensional disturbance introduced in the initial condition decays and the current remains two-dimensional (or axisymmetric) at all times. At the higher two Re, the current becomes fully three-dimensional. The front of the current deforms into a lobe and cleft structure, which undergoes constant rearrangement and leads to uneven front propagation. Our numerical results agree well with experimental observations. The body of the current is strongly three-dimensional and qualitatively resembles a turbulent boundary layer populated with quasi-streamwise and inclined hairpin vortices. These three-dimensional vortical structures have a strong influence on the density field and the interface between the heavy and light fluids is highly distorted.

Three-dimensionality of the current has a strong influence on the propagation speed in the inertial and viscous phases. Two-dimensional approximation substantially underpredicts the mean speed of the current and thus will overestimate the arrival time. In the inertial and viscous phases, the coherent Kelvin–Helmholtz vortices are drawn closer to the front and, thus, influence the speed of the front substantially. On the other hand, in the slumping phase, the coherent vortices are farther upstream of the head of the current and do not affect the front velocity nearly as much. As a consequence, in the slumping phase, both two-dimensional and three-dimensional simulations predict the same propagation speed.

We gratefully acknowledge the support of the Coastal Geosciences Program of the Office of Naval Research (N00014-93-1-0044), the Chicago District of the US Army Corps of Engineers, the Metropolitan Water Reclamation District of Greater Chicago, and National Science Foundation (EAR0609712). Support from the National Center for Supercomputer Applications (NCSA) at the University of Illinois at Urbana-Champaign is also acknowledged. M. I. C. was supported by a Graduate Student Fellowship from the Computational Science and Engineering Program at the University of Illinois at Urbana-Champaign. Dr James Ferry collaborated in the early stages of the computations. Part of the computer time was provided by Dr Fady Najjar and Dr Nahil Sobh. J. R. L. thanks Professor M. Y. Ha for funding support during his visit to the University of Illinois at Urbana-Champaign. M. I. C. wishes to dedicate this work to the memory of Pablo Grinblat and Rubén Ramos,

two great engineers, classmates and friends who left this world when their lives were just starting to flourish.

REFERENCES

Alahyari, A. & Longmire, E. 1996 Development and structure of a gravity current head. *Exps Fluids* **20**, 410–416.

Allen, J. 1985 *Principles of Physical Sedimentology*. Allen & Unwin.

Amy, L., Hogg, A., Peakall, J. & Talling, P. 2005 Abrupt transitions in gravity currents. *J. Geophys. Res.* **110**, F03001, doi: 10.1029/2004JF000197.

Balachandar, S. & Parker, S. 2002 Onset of vortex shedding in an inline and staggered array of rectangular cylinders. *Phys. Fluids* **14** (10), 3714–3732.

Benjamin, T. 1968 Gravity currents and related phenomena. *J. Fluid Mech.* **31**, 209–248.

Birman, V., Martin, J. & Meiburg, E. 2005 The non-Boussinesq lock-exchange problem. Part 2. High-resolution simulations. *J. Fluid Mech.* **537**, 125–144.

Bonnecaze, R. & Lister, J. 1999 Particle-driven gravity currents down planar slopes. *J. Fluid Mech.* **390**, 75–91.

Bonnecaze, R., Huppert, H. & Lister, J. 1993 Particle-driven gravity currents. *J. Fluid Mech.* **250**, 339–369.

Bonnecaze, R., Hallworth, M., Huppert, H. & Lister, J. 1995 Axisymmetric particle-driven gravity currents. *J. Fluid Mech.* **294**, 93–121.

Cantero, M. 2002 Theoretical and numerical modeling of turbidity currents as two-phase flows. MS thesis, University of Illinois at Urbana-Champaign, USA, Urbana, Illinois, USA.

Cantero, M., García, M., Buscaglia, G., Bombardelli, F. & Dari, E. 2003 Multidimensional CFD simulation of a discontinuous density current. In *Proc. XXX IAHR Intl Congress, Thessaloniki, Greece, August 24–29*, pp. 405–412.

Cantero, M., Balachandar, S., García, M. & Ferry, J. 2006 Direct numerical simulations of planar and cyindrical density currents. *J. Appl. Mech.* **73**, 923–930.

Canuto, C., Hussaini, M., Quarteroni, A. & Zang, T. 1988 *Spectral Methods in Fluid Dynamics*. Springer.

Chakraborty, P., Balachandar, S. & Adrian, R. 2005 On the relationships between local vortex identification schemes. *J. Fluid Mech.* **535**, 189–214.

Choi, S.-U. & García, M. 1995 Modeling of one-dimensional turbidity currents with a dissipative-Galerkin finite element method. *J. Hydraul. Res.* **33**, 623–648.

Cortese, T. & Balachandar, S. 1995 High performance spectral simulation of turbulent flows in massively parallel machines with distributed memory. *Intl J. Supercomputer Applic* **9** (3), 187–204.

Daly, B. & Pracht, W. 1968 Numerical study of density-current surges. *Phys. Fluids* **11** (1), 15–30.

Deville, M., Fischer, P. & Mund, E 2002 *High-Order Methods for Incompressible Fluid Flow*. Cambridge University Press.

Droegemeier, K. & Wilhelmson, R. 1986 Kelvin–Helmholtz instability in a numerically simulated thunderstorm outflow. *Bull. Am. Met. Soc.* **67**, 416–417.

Droegemeier, K. & Wilhelmson, R. 1987 Numerical simulation of thunderstorm outflows dynamics. Part I. Outflow sensitivity experiments and turbulence dynamics. *J. Atmos. Sci.* **44**, 1180–1210.

Durran, D. 1999 *Numerical Methods for Wave Equations in Geophysical Fluid Dynamics*. Springer.

Fannelop, T. & Waldman, G. 1971 The dynamics of oil slicks – or 'creeping crude'. *AIAA J.* **41**, 1–10.

Fay, J. 1969 The spreads of oil slicks on a calm sea. In *Oils in the Sea* (ed. David P. Hoult), pp. 53–63.

García, M. 1992 Turbidity currents. In *Encyclopedia of Earth System Science*, pp. 399–408. Academic.

García, M. & Parker, G. 1989 Experiments on hydraulic jumps in turbidity currents near a canyon-fan transition. *Science* **245**, 393–396.

García, M. & Parsons, J. 1996 Mixing at the front of gravity currents. *Dyn. Atmos. Oceans* **24**, 197–205.

Hallworth, M., Huppert, H., Phillips, J. & Sparks, R. 1996 Entrainment into two-dimensional and axisymmetric turbulent gravity currents. *J. Fluid Mech.* **308**, 289–311.

Hallworth, M., Huppert, H. & Ungarish, M. 2001 Axisymmetric gravity currents in a rotating system: experimental and numerical investigations. *J. Fluid Mech.* **447**, 1–29.

Härtel, C., Meiburg, E. & Necker, F. 1999 Vorticity dynamics during the start-up phase of gravity currents. *Il Nuovo Cimento* **22**, 823–833.

Härtel, C., Carlsson, F. & Thunblom, M. 2000*a* Analysis and direct numerical simulation of the flow at a gravity-current head. Part 2. The lobe-and-cleft instability. *J. Fluid Mech.* **418**, 213–229.

Härtel, C., Meiburg, E. & Necker, F. 2000*b* Analysis and direct numerical simulation of the flow at a gravity-current head. Part 1. Flow topology and front speed for slip and no-slip boundaries. *J. Fluid Mech.* **418**, 189–212.

Hoult, D. 1972 Oil spreading in the sea. *Annu. Rev. Fluid Mech.* **4**, 341–368.

Huppert, H. 1982 The propagation of two-dimensional and axisymmetric viscous gravity currents over a rigid horizontal surface. *J. Fliud Mech.* **121**, 43–58.

Huppert, H. 1998 Quantitative modelling of granular suspensions flows. *Phil. Trans. R. Soc. Lond.* A **356**, 2471–2496.

Huppert, H. & Simpson, J. 1980 The slumping of gravity currents. *J. Fluid Mech.* **99**, 785–799.

von Kármán, T. 1940 The engineer grapples with nonlinear problems. *Bull. Am. Math. Soc.* **46**, 615–683.

Lee, B. & Wilhelmson, R. 1997*a* The numerical simulation of non-supercell tornadogenesis. Part I. Initiation and evolution of pretornadic misocyclone circulation along a dry outflow boundary. *J. Atmos. Sci.* **54**, 32–60.

Lee, B. & Wilhelmson, R. 1997*b* The numerical simulation of non-supercell tornadogenesis. Part II. Evolution of a family of tornadoes along a weak outflow boundary. *J. Atmos. Sci.* pp. 2387–2415.

Marino, B., Thomas, L. & Linden, P. 2005 The front condition for gravity currents. *J. Fluid Mech.* **536**, 49–78.

Martin, J. & Moyce, W. 1952*a* Part IV. An experimental study of the collapse of liquid columns on a rigid horizontal bottom. *Phil. Trans. R. Soc. Lond.* A **244**, 312–324.

Martin, J. & Moyce, W. 1952*b* Part V. An experimental study of the collapse of fluid columns on a rigid horizontal bottom, in a medium of lower, but comparable, density. *Phil. Trans. R. Soc. Lond.* A **244**, 325–334.

Metha, A., Sutherland, B. & Kyba, P. 2002 Interfacial gravity currents. II. Wave excitation. *Phys. Fluids* **14**, 3558–3569.

Mittal, R. & Balachandar, S. 1995 Effect of three-dimensionality on the lift and drag of nominally two-dimensional cylinders. *Phys. Fluids* **7**, 1841–1865.

Mittal, R. & Balachandar, S. 1996 Direct numerical simulation of flow past elliptic cylinders. *J. Comput. Phys.* **124**, 351–367.

Necker, F., Härtel, C., Kleiser, L. & Meiburg, E. 2002 High-resolution simulations of particle-driven gravity currents. *Intl J. Multiphase Flow* **28**, 279–300.

Necker, F., Härtel, C., Kleiser, L. & Meiburg, E. 2005 Mixing and dissipation in particle-driven gravity currents. *J. Fluid Mech.* **545**, 339–372.

Özgökmen, T. & Chassignet, E. 2002 Dynamics of two-dimensional turbulent bottom gravity currents. *J. Phys. Oceanogr.* **32**, 1460–1478.

Özgökmen, T., Fischer, P., Duan, J. & Iliescu, T. 2004 Three-dimensional turbulent bottom density currents from a high-order nonhydrostatic spectral element model. *J. Phys. Oceanogr.* **34**, 2006–2026.

Parsons, J. & García, M. 1998 Similarity of gravity current fronts. *Phys. Fluids* **10**, 3209–3213.

Patterson, M., Simpson, J., Dalziel, S. & van Heijst, G. 2006 Vortical motion in the head of an axisymmetric gravity current. *Phys. Fluids* **18** (4), 046601.

Penney, W., Thornhill, C., Fox, L. & Goodwin, E. 1952 Part III. The dispersion, under gravity, of a column of fluid supported on a rigid horizontal plane. *Phil. Trans. R. Soc. Lond.* A **244**, 285–311.

Rottman, J. & Simpson, J. 1983 Gravity currents produced by instantaneous releases of a heavy fluid in a rectangular channel. *J. Fluid Mech.* **135**, 95–110.

Shin, J., Dalziel, S. & Linden, P. 2004 Gravity currents produced by lock exchange. *J. Fluid Mech.* **521**, 1–34.

Simpson, J. 1972 Effects of the lower boundary on the head of a gravity current. *J. Fluid Mech.* **53**, 759–768.

Simpson, J. 1982 Gravity currents in the laboratory, atmosphere, and ocean. *Annu. Rev. of Fluid Mech.* **14**, 213–234.

Simpson, J. 1997 *Gravity Currents*, 2nd edn. Cambridge University Press.

Simpson, J. & Britter, R. 1979 The dynamics of the head of a gravity current advancing over a horizontal surface. *J. Fliud Mech.* **94**, 477–495.

Spicer, T. & Havens, J. 1987 Gravity flow and entrainment by dense gases released instantaneously into calm air. In *Proc. Third Intl Symp. on Stratified Flows Pasadena, California, USA, February 3–5* (ed. E. List & G. Jirka), pp. 642–651.

Terez, D. & Knio, O. 1998*a* Numerical simulation of large-amplitude internal solitary waves. *J. Fluid Mech.* **362**, 53–82.

Terez, D. & Knio, O. 1998*b* Numerical study of the collapse of an axisymmetric mixed region in a pycnoclyne. *Phys. Fluids* **10**, 1438–1448.

Thomas, L., Dalziel, S. & Marino, B. 2003 The structure of the head of an inertial gravity current determined by particle-tracking velocimetry. *Exps Fluids* **34**, 708–716.

Ungarish, M. & Zemach, T. 2003 On axisymmetric rotating gravity currents: two-layer shallow-water and numerical solutions. *J. Fluid Mech.* **481**, 37–66.

Zhou, J., Adrian, R., Balachandar, S. & Kendall, T. 1999 Mechanics for generating coherent packets of hairpin vortices. *J. Fluid Mech.* **387**, 353–396.